Biophysical Characterization of the Sterol Demethylase P450 from *Mycobacterium tuberculosis*, Its Cognate Ferredoxin, and Their Interactions†

Kirsty J. McLean,‡ Ashley J. Warman,§ Harriet E. Seward,§ Ker R. Marshall,§ Hazel M. Girvan,‡ Myles R. Cheesman,|| Michael R. Waterman,⊥ and Andrew W. Munro*,‡

Manchester Interdisciplinary Biocentre, School of Chemical Engineering and Analytical Sciences, University of Manchester, Jackson's Mill, P.O. Box 88, Sackville Street, Manchester M60 1QD, U.K., Department of Biochemistry, University of Leicester, The Henry Wellcome Building, Lancaster Road, Leicester LE1 9NH, U.K., School of Chemical Sciences and Pharmacy, University of East Anglia, Norwich NR4 7TJ, U.K., and Department of Biochemistry, Vanderbilt University School of Medicine, Nashville, Tennessee 37232-0146

Received January 25, 2006; Revised Manuscript Received April 18, 2006

ABSTRACT: *Mycobacterium tuberculosis* encodes a P450 of the sterol demethylase family (CYP51) chromosomally located adjacent to a ferredoxin (Fdx). CYP51 and Fdx were purified to homogeneity and characterized. Spectroscopic analyses were consistent with cysteinate- and aqua-ligated heme iron in CYP51. An ϵ_{419} of 134 mM^{-1} cm^{-1} was determined for oxidized CYP51. Analysis of interactions of 1-, 2-, and 4-phenylimidazoles with CYP51 showed that the 1- and 4-forms were heme iron-coordinating inhibitors, while 2-phenylimidazole induced a substrate-like optical shift. The 2-phenyimidazole-bound CYP51 demonstrated unusual decreases in high-spin heme iron content at elevated temperatures and an almost complete absence of high-spin heme iron by low-temperature EPR. These data suggest thermally induced alterations in CYP51 active site structure and/or binding modes for the small ligand. Reduction of CYP51 in the presence of carbon monoxide leads to formation of an Fe(II)−CO complex with a Soret absorption maximum at 448.5 nm, which collapses (at 0.246 min^{-1} at pH 7.0) forming a species with a Soret maximum at 421.5 nm (the inactive P420 form). The rate of P420 formation is accelerated at lower pH, consistent with protonation of the cysteinate (Cys 394) to a thiol underlying the P450−P420 transition. The P450 form is stabilized by estriol, which induces a type I spectral shift on binding CYP51 (K_d = 21.7 μM). Nonstandard spectral changes occur on CYP51 reduction (using either dithionite or natural redox partners), including a blue-shifted Soret band and development of a strong feature at ∼558.5 nm, suggestive of cysteine thiol ligation. Thus, ligand-free ferrous CYP51 is prone to thiolate ligand protonation even in the absence of carbon monoxide. Analysis of reoxidized CYP51 demonstrates that the enzyme re-forms P450, indicating that Cys 394 thiol is readily deprotonated to thiolate in the ferric form. Spectroscopic analysis of Fdx by EPR (resonance at g = 2.03) and magnetic CD (intensity for oxidized and reduced forms and signal intensity dependence on field strength and temperature) demonstrated that Fdx binds a [3Fe-4S] iron−sulfur cluster. Potentiometric studies show that the midpoint potential for ligand-free CYP51 is −375 mV, increasing to −225 mV in the estriol-bound form. The Fdx potential is −31 mV. Fdx forms a productive electron transfer complex with CYP51 and reduces it at a rate of 3.0 min^{-1} in the ligand-free form and 4.3 min^{-1} in the estriol-bound form, despite a thermodynamic barrier. Steady-state analysis of a *M. tuberculosis* class I redox system comprising flavoprotein reductase A (FprA), Fdx, and estriol-bound CYP51 indicates heme iron reduction as a rate-limiting step.

Mycobacterium tuberculosis (Mtb),[1] the causative agent of tuberculosis (TB), infects approximately one-third of the world's population and causes more deaths worldwide than any other bacterial disease (*1*, *2*). The global threat to human health posed by TB has been exacerbated in recent years by the spread of drug- and multidrug-resistant strains of the pathogen (*3*, *4*). There has also been a synergy by which Mtb has capitalized on the immunocompromised victims of HIV to accelerate its rate of infection worldwide. The alarming spread of Mtb in recent years prompted the World

† The work was funded by the U.K. Biotechnology and Biological Sciences Research Council (BBSRC, Grants C15314, C19757, and BBS/B/06288) and by the EU (Framework V Grant QLK2-CT-2001-02018, X-TB; and Framework VI Grant 01893, NM4TB). A.W.M. and K.J.M. thank the Royal Society for the award of a Leverhulme Trust Senior Research Fellowship.

* To whom correspondence should be addressed. Phone: 0044 161 306 5151. Fax: 0044 161 306 9321. E-mail: Andrew.Munro@Manchester.ac.uk.

‡ University of Manchester.

§ University of Leicester.

|| University of East Anglia.

⊥ Vanderbilt University School of Medicine.

[1] Abbreviations: BV, benzyl viologen; CYP51, sterol demethylase cytochrome P450 from *Mycobacterium tuberculosis*; Fdx, ferredoxin (product of gene *Rv0763c*) from *M. tuberculosis*; FprA, flavoprotein reductase A from *M. tuberculosis*; HNQ, 2-hydroxy-1,4-naphthoquinone; MCD, magnetic circular dichroism; Mtb, *Mycobacterium tuberculosis*; MV, methyl viologen; PMS, phenazine methosulfate; 1-PIM, 1-phenylimidazole; 2-PIM, 2-phenylimidazole; 4-PIM, 4-phenylimidazole; SHE, standard hydrogen electrode.

10.1021/bi0601609 CCC: $33.50
Published on Web 06/15/2006

Health Organization to describe the situation as a potential "global emergency" (*5*, *6*). It is clear that new therapeutics are desperately needed to combat the spread of multidrug-resistant strains of Mtb. No new antitubercular drugs have appeared on the market for more than 40 years, and many existing drugs have undesirable toxic effects (e.g., refs *7*−*9*).

Against this backdrop, a timely development was the determination of the genome sequence of *M. tuberculosis* strain H37Rv by Stewart Cole and co-workers at the Institut Pasteur (*10*, *11*). The genome sequence revealed a preponderance of genes involved in lipid metabolism, as well as a number of other unusual genetic phenomena. Among the most unexpected findings was the fact that Mtb encodes 20 different cytochrome P450 monooxygenases (P450s). By contrast, *Escherichia coli* (with a similarly sized genome) encodes no P450s. Bacterial P450s are traditionally thought to be enzymes involved in catabolic pathways for degradation of unusual carbon sources as metabolic fuel (e.g., ref *12*). However, it is becoming ever clearer that bacterial P450s also play key physiological roles, as evidenced by, for example, the P450 BioI [CYP107H1] enzyme is *Bacillus subtilis* involved in biotin synthesis and by the other fatty acid oxygenases from the same bacterium (*13*−*16*). The large number of P450s in Mtb is mirrored in other mycobacteria and actinomycetes (e.g., *Streptomyces coelicolor*) and implies that at least some of these enzymes have fundamental physiological roles (*17*, *18*). Specifically with regard to the development of novel antitubercular drugs, the preponderance of P450s (and the presence of one particular isoform) in Mtb raises interesting issues pertaining to exploitation of a novel type of drug in anti-Mtb therapy. The azoles (e.g., clotrimazole and fluconazole) are used both topically and orally as antifungals. Their primary fungal target is the lanosterol demethylase P450 CYP51, critical in the synthesis of ergosterol, an essential molecule for fungal membrane integrity (*19*). Until relatively recently, CYP51 was considered to be a P450 confined to eukaryotes. However, the genome sequence of Mtb revealed the first prokaryotic CYP51, encoded by the Mtb H37Rv *Rv0764c* gene (*20*). Moreover, recent studies have indicated that azole antifungals are also potent inhibitors of cell growth in mycobacteria (*17*). Although there is, as yet, no specific evidence to link the anti-mycobacterial activity of azole compounds to inhibition of Mtb CYP51, data demonstrating the tight binding of azoles both to CYP51 and to the Mtb P450 CYP121 have been presented (*21*, *22*). Moreover, the identification of this first prokaryotic CYP51 presented exciting new opportunities for exploring structure−function relationships in the sterol demethylase family. The sequence of Mtb CYP51 is strongly similar to those of the eukaryotic forms, but it lacks the N-terminal membrane anchor region found in the latter enzymes and is thus likely to be a soluble enzyme that is predominantly cytoplasmically located in the pathogen. This provided an excellent opportunity for detailed structural, biophysical, and spectroscopic analysis of a soluble CYP51, perhaps enabling Mtb CYP51 to become a model system for the entire CYP51 family of P450s.

In recent years, Mtb CYP51 has been expressed and partially characterized at the enzyme level, and its atomic structure has been determined in complex with azole drugs and in the presence of the steroid estriol (*21*, *23*, *24*). Mtb CYP51 is located at 858.04 kb on the Mtb H37Rv chromosome, adjacent to a predicted [3Fe-4S] ferredoxin [Fdx, the product of gene *Rv0763c* (*21*)] that, by analogy with other bacterial P450 systems, is likely to be the CYP51 redox partner (e.g., ref *25*). Mtb CYP51 catalyzes oxidative demethylation of dihydrolanosterol and the plant sterol obtusifoliol (*21*), reactions typical of eukaryotic CYP51. However, it appears unlikely that cholesterol or another sterol is a component of the complex Mtb membrane; thus, the physiological role of Mtb CYP51 remains uncertain. In this paper, we report the expression, purification, and characterization of the Mtb ferredoxin encoded by the *Rv0763c* gene, and its biophysical, thermodynamic, and spectroscopic features. In addition, we examine the biophysical properties of Mtb CYP51 and interactions between the P450 and its ferredoxin partner. The data reveal novel aspects relating to the stabilization of CYP51 heme ligation, the nature and properties of the iron−sulfur center in the *Rv0763c*-encoded Fdx, and a thermodynamic barrier to electron transfer between Fdx and CYP51 that may be critical to controlling the catalytic rate in the slow-growing Mtb cells. This study provides fundamental new data relating to the properties and molecular interactaction in this important pathogen P450 system.

EXPERIMENTAL PROCEDURES

Cloning of Mtb CYP51 (Rv0764c), Its Partner Ferredoxin (Rv0763c), and Other Mtb P450 Redox System Genes

CYP51 (gene *Rv0764c*) and the ferredoxin (Fdx, gene *Rv0763c*) were cloned from a Mtb H37Rv cosmid genomic library (from S. Cole at the Institut Pasteur). The Fdx gene was amplified using oligonucleotide primers FdxF (5′-ATGACT**CATATG**GGCTATCGAGTCGAAGCCGACC-GG-3′) and FdxR (5′-ATCCG**GGATCC**TTACTCTCCCG-TTTCTCGGATGG-3′). Restriction enzyme sites for *Nde*I and *Bam*HI, respectively, are in bold. CYP51 was amplified using oligonucleotide primers CYP51F (5′-TATGACT**CATATG**AGCGCTGTTGCACTACC-3′) and CYP51R (5′-AAGA-C**AAGCTT**AAACTCCCGTTCGCCGG-3′). Restriction sites for *Nde*I and *Hin*dIII, respectively, are in bold. Start codons are underlined. PCR conditions were an initial denaturation step of 95 °C (60 s), followed by 30 cycles of (a) denaturation at 95 °C for 20 s, (b) annealing at 55 °C for 30 s, and (c) polymerization at 72 °C for 60 s. The PCR was completed with a polymerization step of 72 °C for 10 min. CYP51 PCR conditions were like those for Fdx, with the exception that step c was for 120 s. PCRs were carried out in a Techne PHC-2 thermal cycler. PCR mixes contained ∼10 ng of template Mtb cosmid DNA, 0.2 μM primers (10 pmol), 0.2 mM dNTPs, 1.5 mM $MgCl_2$, and 2 units of *Taq* polymerase, in a total volume of 50 μL overlaid with nuclease-free mineral oil (Sigma). PCR products were resolved on 1% agarose gels. PCR fragments were excised from the gel and purified using the Qiaex II gel extraction kit (Qiagen, West Sussex, U.K.). Purified DNA was cloned directly into plasmid vector pGEM-T (Promega) using standard procedures (*26*). Successful recombinants were identified by blue/white color selection from transformants grown on X-gal- and IPTG-containing LB agar with ampicillin (100 μg/mL) (*26*). Plasmids were prepared from a transformant culture using an FX DNA purification kit (Pharmacia), and the presence of CYP51 and Fdx genes was verified by restriction

digestion with *Nde*I/*Hin*dIII and *Nde*I/*Bam*HI, respectively. DNA sequencing of clones (Applied Biosystems DNA sequencer and Universal primers) confirmed correct gene sequences. CYP51 and Fdx genes were excised (as before) and cloned into expression vectors pET20b and pET11a, respectively. An alternative construct expressing the Fdx gene from vector pET17b was also used, as described previously (*21*). This clone produces a four-histidine C-terminally tagged version of Fdx. Cloning, expression, and characterization of the Mtb adrenodoxin reductase homologue enzyme flavoprotein reductase A (FprA, product of Mtb gene *Rv3106*) were described previously (*27*). Cloning and expression of Mtb P450 CYP121 have also been described previously (*28*).

Expression and Purification of Mtb CYP51 and Fdx

For both CYP51 and Fdx genes, expression in *E. coli* is under control of a T7 RNA polymerase promoter in pET20b and pET11a vectors, respectively. CYP51 was expressed in *E. coli* strain HMS174 (DE3) by growth at 30 °C overnight in LB medium with IPTG (1 mM) induction at an OD_{600} of 0.9. Cells (10 L) were collected by centrifugation (5000*g* for 20 min at 4 °C). Cell pellets were washed by being resuspended in 50 mM Tris-HCl and 1 mM EDTA (buffer A), pooled, and repelletted as previously described. The final pellet was resuspended in a minimal volume of ice-cold buffer A containing protease inhibitors [phenylmethanesulfonyl fluoride (PMSF) and benzamidine hydrochloride, both at 1 mM], and cells were broken by sonication on ice (6×20 s bursts at 45% full power on a Bandelin Sonopuls instrument, with a 5 min cooling time between pulses) followed by passage through a French press (two passes at 950 lb/in.^{2}). Broken cells were centrifuged to pellet cell debris (18000*g* for 40 min at 4 °C), and the extract was diluted in buffer A and loaded directly onto a DEAE ion-exchange column prior to elution in a linear gradient with buffer A containing 500 mM KCl. Heme-containing fractions were pooled, dialyzed into buffer A, and purified on Q-Sepharose and hydroxyapatite columns, as described for Mtb CYP121 (*22*). Final fractions were analyzed for purity spectrophotometrically and pooled. Purified protein was dialyzed into 10 mM Tris-HCl (pH 7.5) to desalt, concentrated, and stored at −80 °C. Both versions of Mtb Fdx were expressed in Origami (DE3) cells grown in Terrific broth (*26*). Cultures (6 L) were grown at 25 °C overnight without IPTG induction. Cells of the non-tagged version of Fdx were disrupted as described above, and protein was purified by successive chromatography steps on DEAE-Sephacel and Q-Sepharose. Protein was loaded in buffer A and eluted using a linear gradient from 0 to 500 mM KCl in buffer A. Fractions were pooled, concentrated, and further resolved on a G-25 Sephadex gel filtration column. The His-tagged Fdx was purified using a nickel−NTA affinity column (Novagen). Cell extract was prepared in 50 mM potassium phosphate (7.5) containing 10% (v/v) glycerol, 60 μM imidazole, and 100 μM NaCl and loaded directly onto the nickel column. The column was washed extensively before elution with the same buffer with 250 μM imidazole. Fractions were pooled, dialyzed, and passed through the column again. This time, fractions with the highest purity (by A_{412}/A_{280} ratio) were concentrated by ultrafiltration (Centriprep 3 kDa cutoff, Millipore) and applied to the G-25 Sephadex column as before. Finally, both versions of Fdx were dialyzed into 50 mM potassium phosphate (pH 7.5) containing 50% (v/v) glycerol and stored at −80 °C. FprA and CYP121 were expressed and purified as described previously (*22*, *27*, *28*).

Spectroscopic Analysis

UV−visible spectroscopic analysis of Fdx and CYP51 was carried out on a Cary 50 UV−visible spectrophotometer (Varian). Optical titrations to determine K_d values for CYP51 ligands were carried out at 30 °C using CYP51 at 1−5 μM and with ligands (lanosterol, estriol, testosterone, imidazoles, or azole drugs) solubilized in the appropriate solvent (*22*). The final solvent concentration was maintained at <1% of the final volume of the assay mixture. K_d values in all cases were computed by fitting data for ligand-induced absorption change versus the relevant ligand concentration to either a rectangular hyperbola or (for tight-binding azole ligands) to a quadratic function (eq 1)

$$A_{obs} = (A_{max}/2E_t)(S + E_t + K_d) - \{[(S + E_t + K_d)^2 - (4SE_t)]^{0.5}\} \quad (1)$$

where A_{obs} represents the observed absorption difference at each ligand addition, A_{max} is the maximal absorption difference at ligand saturation, E_t is the total enzyme concentration, and S is the ligand concentration. Equation 1 is used to describe binding of ligands where the K_d value is similar in magnitude to the concentration of enzyme used, in which case substantial amounts of enzyme (E) and ligand (S) are consumed in the E·S complex as the titration progresses. All data fitting was done using Origin (Microcal).

Circular Dichroism Spectroscopy

CD spectra of Fdx and CYP51 were recorded at 20 °C using a JASCO J600 spectrapolarimeter. Far-UV CD spectra were recorded from 190 to 260 nm in a quartz cylindrical cell with a path length of 0.02 cm and with a scan rate of 10 nm/min. Near-UV and visible CD spectra were recorded between 260 and 320 nm and between 320 and 600 nm, respectively, in cells with a path length of 0.5 cm with scan rates of 20 nm/min. Spectra were recorded in duplicate and averaged. Fdx and CYP51 protein concentrations used were 35 and 2 μM in the far-UV CD region and 285 and 20 μM in the near-UV−visible region, respectively.

EPR Spectroscopy

Electron paramagnetic resonance (EPR) spectra of Fdx and CYP51 were recorded on a Bruker ER-300D series electromagnet and microwave source interfaced with a Bruker EMX control unit and fitted with an ESR-9 liquid helium flow cryostat (Oxford Instruments), and a dual-mode microwave cavity from Bruker (ER-4116DM). Spectra were recorded at 10 K with a microwave power of 2.08 mW and modulation amplitudes of 2.1 and 10 G for Fdx and CYP51, respectively. Protein samples were contained in 50 mM potassium phosphate (pH 7.5). Fdx (800 μM) spectra were recorded for oxidized and sodium dithionite-reduced forms (dithionite at a 10-fold molar excess). CYP51 (200 μM) spectra were recorded in the absence and presence of near-saturating amounts of putative heme ligands 2- and 4-phenylimidazole (as observed by spectral analysis of complexes) and of the azole drug fluconazole, which was added stepwise as a solid

to the protein solution and equilibrated until no further spectral changes were observed.

MCD Spectroscopy

Magnetic circular dichroism (MCD) spectra were recorded on circular dichrographs, JASCO J-500D and JASCO J-730, for ranges of 280−1000 and 800−2000 nm, respectively. Samples were mounted on an SM-1, 6 T superconducting solenoid (Oxford Instruments) with an ambient-temperature bore for measurements at room temperature. Samples were prepared in deuterated 50 mM HEPES (pH 7.5). Low-temperature MCD spectroscopy of oxidized and dithionite-reduced Fdx (270 μM) in the presence of 50% glassing agent was done with the split-coil variable-temperature SM-4 magnet (Oxford Instruments) at 10, 4.2, and 1.7 K. Initial measurements were performed at 5 T. Further experiments were carried out at each of the three temperatures, increasing the applied magnetic field strength stepwise from 0.02 to 1 $\beta B/2kT$.

Resonance Raman

A resonance Raman spectrum of CYP51 was obtained using 15 mW, 406.7 nm radiation at the sample, from a Coherent Innova 300 krypton ion laser, and acquired using a Renishaw micro-Raman system 1000 spectrophotometer. The sample was held in a capillary under the microscope at a concentration of 50 μM, and an extended scan was obtained from 200 to 1700 cm^{-1}, with 12 $\times$ 15 s exposures.

Potentiometric Studies

Redox titrations were performed in a Belle Technology glovebox under a nitrogen atmosphere, as described previously (*29*−*31*). The protein solution (approximately 6−12 μM for P450s in 5 mL of buffer) was titrated electrochemically by the method of Dutton (*29*) using sodium dithionite as a reductant and ferricyanide as an oxidant. Mediators were added to facilitate electrical communication between enzyme and electrode, prior to titration. Typically, 2 μM phenazine methosulfate (PMS), 7 μM 2-hydroxy-1,4-naphthoquinone (HNQ), 0.3 μM methyl viologen (MV), and 1 μM benzyl viologen (BV) were included (to mediate in the range from 100 to −480 mV) (*30*, *31*). Spectra (250−800 nm) were recorded using a Cary UV-50 Bio UV−visible scanning spectrophotometer. The electrochemical potential of the solution was measured using a Hanna pH 211 meter coupled to a Pt/Calomel electrode (ThermoRussell Ltd.) at 25 °C. The electrode was calibrated using the Fe^{3+}/Fe^{2+} EDTA couple as a standard (108 mV). A factor of 244 mV was used to correct relative to the standard hydrogen electrode. The redox titration of Fdx (63 μM in 5 mL of buffer) was carried out in the presence of 10% (v/v) glycerol to aid stability. Further redox titrations were performed with Fdx (40 μM) in the presence of CYP51 (10 μM). The experiment was then repeated exactly as before in the presence of CYP121 (also 10 μM). Further redox titrations were performed with CYP51 bound to either estriol (90 μM) or 2-PIM (7.5 mM). Redox titrations were performed in both reductive and oxidative directions to ensure that the redox processes were fully reversible and that no hysteretic effects were observed.

Thermal Effects on CYP51 Optical Spectra

To examine thermally induced changes in heme iron spin-state equilibrium, spectra for CYP51 in substrate-free and estriol- and 2-PIM-bound forms were recorded across a temperature range of 5−50 °C. A 1 mL solution of CYP51 (~0.75−2 μM) was prepared in 50 mM Tris-HCl (pH 7.2). A reference spectrum was collected at 30 °C (following equilibration) using a Cary UV-50 Bio spectrophotometer fitted with a Peltier accessory. Thereafter, the temperature was decreased stepwise with spectra recorded at 2 °C intervals after 2 min equilibration periods at each temperature. The solution was then heated progressively, and spectra were again recorded at 2 °C intervals. Above 50 °C, protein aggregation and precipitation were observed, and experiments were terminated at this point. The procedure was repeated in the presence of 87 μM estriol or 7.5 mM 2-phenylimidazole. These concentrations approach enzyme saturation without causing excessive turbidity. To analyze data, difference spectra were created by subtracting the initial (lowest temperature) spectrum from all subsequent spectra. The absorbance minima of spectral troughs (~423 nm) were subtracted from the absorbance peak maxima (~389 nm). Absorption change values were plotted against temperature to determine differences in the behavior of ligand-free and ligand-bound forms of CYP51.

Kinetic Analysis

Transient Kinetics. To determine rates of electron transfer between Mtb Fdx and CYP51 in the absence of ligands and in the presence of estriol and 2-PIM, stopped-flow studies of electron transfer between the Fdx iron−sulfur cluster and the CYP51 heme iron were performed. The rate of single-electron transfer from Fdx to CYP51 was measured by stopped-flow absorption on an Applied Photophysics SX18MV UV−visible stopped-flow instrument coupled to a photodiode array UV−visible detector. Experiments were carried out under anaerobic conditions in a Belle technology glovebox with oxygen levels of <2 ppm. Fdx and CYP51 were prepared separately in anaerobic 50 mM potassium phosphate (pH 7.5) saturated with carbon monoxide. CYP51 solutions (5 μM) were also titrated with estriol and 2-phenylimidazole (final concentrations of 50 μM and 3 mM, respectively) to convert the P450 to an extensively high-spin form. Immediately prior to stopped-flow mixing, Fdx was reduced by titration with sodium dithionite, using the minimal amount of reductant to fully reduce the Fe−S cluster. Excess dithionite was removed by gel filtration on a Bio-Rad 10DG desalting column, and Fdx was checked spectroscopically to ensure full reduction. Stopped-flow mixing of reduced Fdx (20 μM) with CYP51 (2.5 μM) was performed at 30 °C. Entire spectra were recorded (750−250 nm) using the photodiode array facility. Control experiments were carried out with identical samples of Fdx or CYP51 mixed with a buffer blank, to rule out any significant changes resulting form photobleaching. The rate of electron transfer from Fdx to CYP51 in the absence and presence of 2-phenylimidazole and estriol was followed using the formation of the ferrous−CO complex of the P450, resulting in absorption development at 448 nm. Rates were determined either by fitting ΔA_{448} data to an exponential function or by fitting entire spectral changes observed using the global analysis ProKin software (Applied Photophysics). Both procedures generated essentially identical results for the rate of P450 formation. The rate of collapse of P450 to P420 was determined from global analysis using a two-step kinetic model using ProKin.

Steady-State Kinetic Analysis. The capacity of the entire Mtb class I redox system (comprising FprA and Fdx) to transfer electrons to CYP51 was examined by steady-state analysis of NADPH oxidation. A cuvette solution containing a mixture of 2 μM FprA, 5 μM CYP51, and varying amounts of the Fdx (0−40 μM) was prepared in aerobic 50 mM potassium phosphate (pH 7.5). Steady-state NADPH oxidation was assessed either using substrate-free CYP51 or CYP51 bound to estriol (50 μM) or 2-PIM (3 mM). The reaction was initiated by addition of NADPH (200 μM), and the absorption change at 340 nm (ϵ_{340} = 6210 M^{-1} cm^{-1}) was followed for up to 10 min. Initial reaction rates were determined in triplicate at each Fdx concentration. Data (initial rate vs Fdx concentration) were fitted to rectangular hyperbolae to derive the apparent binding constants (K_d) for Fdx and the limiting turnover rate (apparent k_{cat}) for the systems that were studied.

CYP51−CO Adduct Collapse

Conversion of the CYP51 Fe(II)−CO complex from the "native" form with a Soret band maximum close to 450 nm (P450) to the "inactive" form with a maximum near 420 nm (P420) was monitored spectrophotometrically in the presence and absence of exogenous ligands. Solutions of CYP51 (~2−4 μM) were prepared in 100 mM Tris-HCl (pH 7.2), and UV−visible absorption spectra were recorded for the oxidized species on a Cary UV-50 Bio spectrophotometer at 25 °C. CYP51 solutions were reduced using a small amount of sodium dithionite and bubbled briefly with carbon monoxide to form the P450−CO complex. Spectra were then recorded every 30 s for up to 1 h to observe changes as the P450 collapsed into the P420 form. The stability of the CYP51−CO complex was also examined in the same way in the presence of estriol (87 μM) and 2-phenylimidazole (7.5 mM). Plots of the absorbance change at 448 or 420 nm against time were generated and data fitted to an exponential function to derive rate constants for the process of P450-to-P420 collapse. To examine the effects of pH on the process of P420 collapse, similar studies were carried out for ligand-free CYP51 in the same buffer for the pH range of 6.0−9.0 at 0.5 pH unit increments. To assess whether ligand addition could reverse P420 formation, estriol (87 μM) was added to a sample of freshly prepared P420 (as described above) and spectra were collected at 5 min intervals for several additional hours. The experiment was repeated at a low temperature (15 °C) and in the presence of 10% (v/v) glycerol.

RESULTS

Cloning and Genetic Context of CYP51 and Its Cognate Ferredoxin Fdx

The Mtb H37Rv genome sequence demonstrated that only two CYP genes were located adjacent to predicted ferredoxins that might act as typical class I P450 redox partners and, possibly, be cotranscribed with the P450 itself (*1*). *Rv1786* encodes a putative [3Fe-4S] ferredoxin and is located immediately adjacent to CYP143 (*Rv1785c*). This gene pair is divergent on the chromosome. The P450 encoded by *Rv0764c* (CYP51) is immediately followed on the same strand by the putative [3Fe-4S] ferredoxin Fdx (*Rv0763c*). Previous studies reported expression of these proteins in *E. coli*, and the atomic structure of Mtb CYP51 was determined in the presence of the azole inhibitors fluconazole and 4-phenylimidazole, and more recently in complex with estriol and in the ligand-free form (*23*, *24*). In the proximity of CYP51 and Fdx is another P450 (CYP123, *Rv0766c*) of unknown function, immediately downstream from *Rv0767c*, encoding a putative transcriptional regulatory protein. Both CYP123 and the putative regulator are upregulated at the mRNA level by high temperatures, suggesting a possible role in heat shock response (*32*). A putative oxidoreductase protein (product of *Rv0765c*) separates CYP51 and CYP123. Downstream of CYP51 is a cluster of proteins of uncertain function, including a putative alcohol dehydrogenase (*adhB*, *Rv0759c*). The genetic proximity of the two P450s and the putative redox partner ferredoxin Fdx may suggest their involvement in a common metabolic process. However, genetic context does not provide sufficient information to indicate the nature of this role. Mtb CYP51 demethylates sterol substrates, but the pathogen may not synthesize sterols de novo, perhaps pointing to an alternative cellular role. To characterize the Mtb Fdx protein, its interactions with CYP51, and the spectroscopic, kinetic, and thermodynamic features of these proteins, the *Rv0763c* (Fdx) and *Rv0764c* (CYP51) genes were cloned in *E. coli* expression vectors as described in Experimental Procedures.

Protein Purification, UV−Visible Spectral, and Ligand Binding Properties of Mtb CYP51 and Fdx

Mtb CYP51. Mtb gene *Rv0764c* (CYP51) was expressed from an inducible T7 promoter system in plasmid vector pET20b in *E. coli* HMS174 (DE3) cells, and the encoded P450 protein was purified to homogeneity in three steps using DEAE and Q-Sepharose ion-exchange resins and chromatography on hydroxyapatite. Pure ferric CYP51 has a typical P450 UV−visible spectrum, with a Soret band at 419 nm, and Q-bands (or α and β bands) at ~572 and 535 nm, respectively (Figure 1A). These features are similar to those seen previously for the other structurally characterized Mtb P450 CYP121 (maxima at 565, 538, and 416.5 nm) (*22*). In CYP51 (as with CYP121), the absence of any significant absorption shoulder at ~390 nm indicates that the P450 is predominantly low-spin ($S = {}^1/_2$) with minimal high-spin ($S = {}^5/_2$) ferric heme iron content. This conclusion is supported by EPR (see below). For pure CYP51, the ratio of Soret absorption to the protein band at 280 nm (the *R*/*z* ratio) is ~1.8 (A_{419}/A_{280}). Low-spin ferric P450s are cysteinate-ligated (the ligand is Cys 394 in CYP51) with a weakly bound water molecule as the other heme iron axial ligand. The water is displaced by stronger ligands, leading to optical perturbations. Figure 1A shows spectra associated with coordination of imidazole (Soret λ_{max} = 424 nm), cyanide (λ_{max} = 435.5 nm), and nitric oxide (λ_{max} = 434 nm). In the NO-bound form (as with CYP121), increases in absorption and shifts in position of the Q-bands (particularly the β band) are observed. Optical titrations with cyanide and imidazole produced K_d values of 18.8 ± 3.1 and 11.7 ± 0.9 mM, respectively (Table 1). Weak binding of these polar molecules is consistent with the hydrophobic nature of the CYP51 active site and probably also with the strong electron-donating effect of the proximal thiolate ligand. Bulkier and more hydrophobic azole drugs are more potent inhibitors of

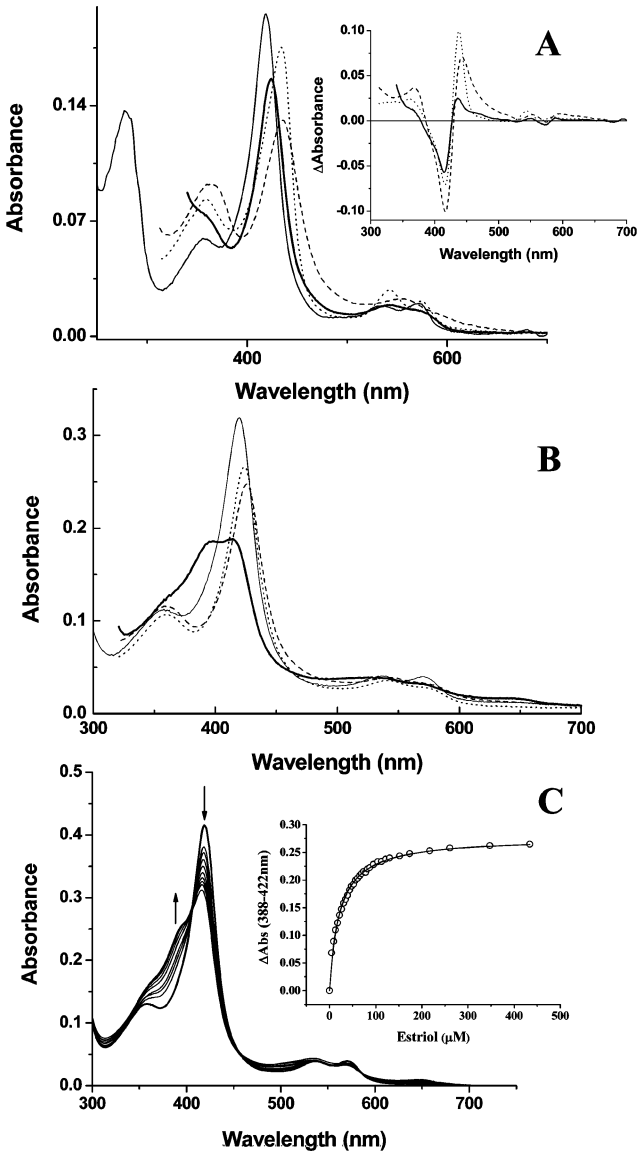

FIGURE 1: UV−visible absorption and ligand binding properties of Mtb CYP51. (A) Absorption spectra of oxidized Mtb CYP51 (1.45 μM, thin solid line, A_{max} = 419 nm) and Mtb CYP51 in complex with imidazole (thick solid line, A_{max} = 424 nm), cyanide (dashed line, A_{max} = 435.5 nm), and nitric oxide (dotted line, A_{max} = 434 nm). By comparison with the extinction coefficient of CYP51 (ϵ_{419} = 134 000 M^{-1} cm^{-1}), the coefficients for the CYP51 adducts at their relevant spectral maxima are as follows: ϵ_{424} = 107 000 M^{-1} cm^{-1} (imidazole), $\epsilon_{435.5}$ = 90 000 M^{-1} cm^{-1} (cyanide), and ϵ_{434} = 120 000 M^{-1} cm^{-1} (nitric oxide). The inset shows diference spectra induced by subtraction of the ligand-free spectrum from those of the relevant complexes (solid line, imidazole complex; dashed line, cyanide complex; dotted line, nitric oxide complex). (B) Spectral features of CYP51 complexes with different phenylimidazoles: thin solid line, ligand-free CYP51 (2.35 μM); thick solid line, 2-PIM-bound CYP51 (7.5 mM ligand); dotted line, 1-PIM-bound CYP51 (3.2 μM ligand); and dashed line, 4-PIM-bound CYP51 (1.2 mM ligand). Soret spectral maxima are at ~425 nm for 1-PIM and 4-PIM, but the 2-PIM-bound form shows high-spin character with Soret maxima at ~414 and 395 nm. (C) Spectral titration of CYP51 (3.1 μM) with estriol. Estriol induces a shift in the spectral maximum from 419 to ~390 nm. Spectra are shown for ligand-free CYP51 (thick solid line) and for estriol complexes at 4.3, 8.7, 13.0, 17.4, 26.0, 34.7, 43.4, 47.7, and 52.1 μM (thin solid lines, progressive Soret shift toward 390 nm, as indicated by arrows). The inset shows a plot of the induced CYP51 spectral shift ($A_{388} - A_{422}$) vs the relevant concentration of estriol (micromolar). Data are fitted to a hyperbolic function, producing a K_d value of 21.7 ± 0.8 μM.

CYP51 (see below). The unusual properties of the ferrous−carbon monoxy complex of CYP51 are also detailed below.

While relative intensities of the aqua-ligated and NO-ligated CYP51 Soret bands are similar to those in other P450s [e.g., P450 BM3 (*33*)], intensities of the cyanide-ligated and (particularly) the imidazole-ligated Soret bands are quite low (Figure 1A). To verify that this phenomenon is associated with low adduct extinction coefficients, spectra were recorded for CYP51 bound to either imidazole or cyanide at their apparent K_d concentrations. Thereafter, samples were diluted 2-, 4-, and 8-fold into ligand-free buffer, and spectra were recorded at each dilution. These spectra indicated that binding of these ligands is freely reversible and that the Soret band increases in intensity as it returns to the ligand-free form. Thus, imidazole- and cyanide-ligated CYP51 species have low Soret coefficients. A typical method for determining P450 concentrations relies on formation of the Fe(II)−CO adduct, and application of the extinction coefficient $\epsilon_{450-490}$ of 91 mM^{-1} cm^{-1} for data from the reduced/CO-bound minus reduced P450 difference spectrum (*34*). For Mtb CYP51, the instability of the CO complex prevents accurate use of this method. Moreover, reduction of CYP51 results in a spectral shift that suggests the nature of the proximal ligand has changed (see below). Instead, we determined the heme concentration by the pyridine hemochromagen technique (*35*). This indicated an ϵ_{419} coefficient of 134 mM^{-1} cm^{-1} for oxidized CYP51 at the Soret peak. This value is similar to that determined by the same method for the cineole-degrading P450cin (CYP176A) from *Citrobacter braakii* [ϵ_{415} = 150 mM^{-1} cm^{-1} (*36*)]. By comparison with that of oxidized, ligand-free CYP51, Soret coefficients for the cyanide and imidazole adducts are as follows: $\epsilon_{435.5}$ = 90 mM^{-1} cm^{-1} and ϵ_{424} = 107 mM^{-1} cm^{-1}, respectively. The value for the nitrosyl adduct (ϵ_{434}) is 120 mM^{-1} cm^{-1}.

Binding of a substituted imidazole [2-phenylimidazole (2-PIM)] to Mtb CYP51 was shown to induce a substrate-like spectral change, with a decrease in the intensity of the Soret band in the 2-PIM complex and a shift of the Soret maximum to 396 nm, concomitant with the accumulation of high-spin heme iron (*37*). This finding was confirmed, and a considerable decrease in Soret intensity was again observed in the 2-PIM-bound complex. These features were distinct from those for 1-PIM and 4-PIM complexes. Here, the Soret band shifted to ~425 nm (similar to the imidazole complex) at apparent saturation (Figure 1B). As with imidazole, there is a substantial decrease in Soret absorption on complexation with these azoles. Thus, both 1-PIM and 4-PIM act as inhibitors and coordinate to the CYP51 heme iron, reinforcing the low-spin state of the heme iron, whereas 2-PIM instead likely binds in the active site distal to the heme iron and displaces a water molecule weakly bound to the iron, resulting in electronic reorganization in the heme iron d-orbitals and an increased high-spin population. Spectral titrations with phenylimidazoles were performed and K_d values determined by fitting induced absorption change versus ligand concentration data to hyperbolae, producing values of 0.44 ± 0.07 μM (1-PIM), 3.19 ± 0.37 mM (2-PIM), and 452 ± 27 μM (4-PIM). Thus, while both 1-PIM and 4-PIM produce type II inhibitor-like shifts in the heme spectrum, 1-PIM binds much tighter (~10^3-fold) to CYP51 than does 4-PIM. 2-PIM produces a substrate-like type I spectral shift and binds even more weakly (a further ~7-

Table 1: Spectroscopic and Thermodynamic Properties of *Mycobacterium tuberculosis* CYP51[a]

	CYP51	CYP121	CYP102A1	CYP101
UV−visible absorption Soret (nm); ϵ (mM^{-1} cm^{-1})				
Fe^{3+}	419; 134	416.5; 110	419; 95	417; 115
Fe^{3+}−NO	434; 120	437; 102	435; 86	430; 103
Fe^{3+}−CN	435.5; 90	438; 95	445; 57	439; 78.5
Fe^{3+}−imidazole	424; 107	424; 108	425; 104	425; 98
EPR (*g* values for the low-spin form)	2.44, 2.25, 1.91	2.47, 2.25, 1.90	2.42, 2.26, 1.92	2.44, 2.25, 1.91
E_m with/without substrate (mV vs SHE)	−375/−225	∼−450	−427/−289	−330/−162
resonance Raman (cm^{-1} for ν_2, ν_3, ν_4 and ν_{10} for the low-spin enzyme)	1583, 1504, 1373, 1638	1577, 1500, 1372, 1631	1581, 1499, 1372, 1636	1569, 1487, 1370, 1622

[a] The features of Mtb CYP51 are compared with those for the Mtb CYP121 enzyme and with those for the prototypical prokaryotic enzymes *Bacillus megaterium* P450 BM3 (CYP102A1, heme domain) and *Pseudomonas putida* P450 cam (CYP101). The following data are presented: (i) the Soret spectral maximum (and the extinction coefficient) for the low-spin (Fe^{3+}) forms and for the nitric oxide (Fe^{3+}−NO), cyanide (Fe^{3+}−CN), and imidazole (Fe^{3+}−imidazole) complexes, (ii) the *g* values for the low-spin (substrate-free) forms from EPR, (iii) the midpoint heme iron Fe^{3+}/Fe^{2+} reduction potential (E_m), and (iv) major resonance Raman features (key oxidation, coordination, and spin-state markers) for the substrate-free, low-spin enzymes (ν_2−ν_4 and ν_{10}). Redox potential data are for CYP51 in the absence of substrate and bound to estriol (this work), for CYP121 in the substrate-free form (*21*), for CYP102A1 in substrate-free and arachidonate-bound forms (*55*), and for CYP101 in substrate-free and camphor-bound forms (*56*). UV−visible data are from refs *21* and *68*−*72*. EPR data are from refs *21*, *68*, and *70*−*72*. Resonance Raman data are from refs *21*, *37*, *68*, and *73*.

fold compared to 4-PIM). While the sterols lanosterol and obtusifoliol are demethylated by Mtb CYP51, titrations with these compounds produce only marginal spectral shifts within their solubility range in aqueous buffer. By contrast, estriol produces a substantial CYP51 heme spectral change toward 392 nm, consistent with formation of a high-spin state. From spectral titration with estriol, the K_d was determined to be 21.7 ± 0.8 μM (Figure 1C).

Fungal CYP51 enzymes are targets for azole and triazole drugs. Binding of Mtb CYP51 to a range of clinically relevant azoles was analyzed by spectrophotometric titration. The K_d values were determined as follows, compared (in parentheses) with azole K_d values measured for CYP121, the only other structurally characterized Mtb P450: 0.18 ± 0.02 μM (0.07 ± 0.03 μM) for clotrimazole, 0.31 ± 0.04 μM (0.03 ± 0.02 μM) for econazole, 5.82 ± 0.12 μM (9.70 ± 0.60 μM) for fluconazole, 3.57 ± 0.25 μM (3.30 ± 0.30 μM) for ketoconazole, and 0.20 ± 0.04 μM (0.09 ± 0.05 μM) for miconazole. Clearly, both Mtb isoforms have a high affinity for polycyclic azoles. Miconazole and clotrimazole bind tightest to CYP51, although the affinity of CYP121 for both these azoles and for econazole is significantly higher than that of CYP51.

Mtb Fdx. The Fdx-encoding gene (*Rv0763c*) was expressed as both a non-tagged protein in plasmid vector pET11a and a His-tagged protein in vector pET17b (*21*). Fdx is predicted to be a 68-amino acid protein (including the initiator methionine) from the genome sequence. This was confirmed by sequencing of the cloned *Rv0763c* gene (not shown). Tagged Fdx has four additional histidines at the C-terminus. Spectral and thermodynamic properties of both forms were essentially identical, but the His-tagged protein could be purified in a much larger yield as a result of both higher expression levels and the affinity purification step (on Ni−NTA resin) that was used. For this reason, spectroscopic and kinetic studies reported herein relate to studies with the His-tagged Fdx. Fdx protein was purified by two successive rounds of affinity chromatography on Ni−NTA resin (Novagen) followed by gel filtration to desalt the sample and to remove minor contaminants. On the basis of an extinction coefficient of 11 300 M^{-1} cm^{-1} at 412 nm, Fdx is purified in these three steps at a level of 9 ± 1 mg of protein/L of cell culture. This compares with <2 mg/L from

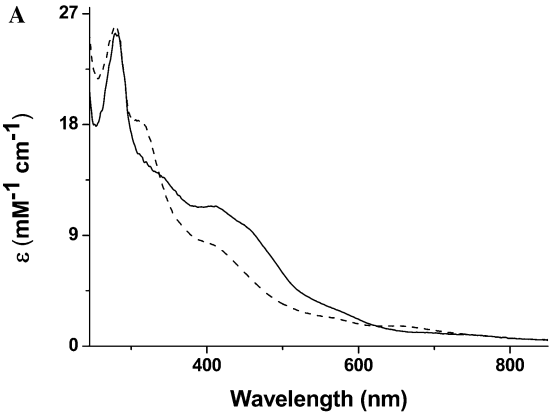

B

```
Mtb     --------MGYRVEADRDLCQGHAMCELEAPEYFRVP-KRGQVEILDPEPPEEARGVIKH 51
Mbov    --------MGYRVEADRDLCQGHAMCELEAPEYFRVP-KRGQVEILDPEPPEEARGVIKH 51
Noc     ----------MKIVADYDKCEGLGMCEAMAPEFFEVQ-DEG----LDEHPLDEEHRTGKA 45
Slav    ----------MEIRIDRDKCVSGGVCAMFAPQVFDQD-DEGMGVVDNSAPAEEIAAAVRS 49
Sco     MTLAGQAFGSGRVGAERDRCVGAGQCVLAAPGVFDQDEEDGLVRVLAERPSAAESDAVRA 60
Msmeg   ----------MRVSVDLNRCQDHGQCVIAAPSVFSMT-DDG--VLEYQVGVESERFAVEE 47
                  .:  : : * . . *   **  *    . *              . .

Mtb     AVWACPTQALSIRETGE------ 68
Mbov    AVWACPTQALSIRETGE------ 68
Noc     AVDACPVLALS------------ 56
Slav    VVWRCPGHAISVHEQEVERGGRR 72
Sco     AVRACPSGALTLR---------- 73
Msmeg   AADVCPLQAITIED--------- 61
        ..  **  *::
```

FIGURE 2: Properties of Mtb Fdx. (A) UV−visible absorption spectra and extinction coefficients for oxidized (solid line) and sodium dithionite-reduced (dashed line) forms of Fdx. (B) Amino acid alignment of the Mtb Fdx sequence (Mtb) with those of predicted [3Fe-4S] ferredoxins from *Mycobacterium bovis* (Mbov), *Nocardioides* spp. strain CF8 (Noc), *Streptomyces lavendulae* (Slav), *Streptomyces coelicolor* (Sco). and *Mycobacterium smegmatis* (Msmeg). Alignment was performed using ClustalW via the EBI server (http://www.ebi.ac.uk/cgi-bin/clustalw). Identical residues are denoted with asterisks. Similar amino acids are indicated by single or double dots (according to the level of similarity). Mtb Fdx is identical in amino acid sequence to its *M. bovis* homologue (*Mb0786c*) but is only 33% identical (across 61 residues) with its shorter homologue from *M. smegmatis*.

the non-tagged construct. Pure Fdx has a distinctive dark green/brown color and a broad UV−visible spectrum in its oxidized form with a peak at 412 nm and pronounced absorption shoulders at ∼460 and ∼580 nm (Figure 2A and Table 2). The aromatic amino absorption band is at 280 nm, and a further shoulder is seen at ∼340 nm. For homogeneous Fdx, the A_{278}/A_{412} absorption ratio is ∼2.2. Reduction of Fdx by dithionite led to loss of the green/brown color and to bleaching of the spectrum between ∼350 and 600 nm. At longer wavelengths (∼600−750 nm), Fdx exhibits increased

Table 2: Spectroscopic and Thermodynamic Properties of *M. tuberculosis* Fdx[a]

	Fdx	Fd1	Fd2	putidaredoxin	Fer
host organism	*M. tuberculosis*	*Streptomyces griseolus*	*St. griseolus*	*Ps. putida*	*B. subtilis*
iron−sulfur cluster	[3Fe-4S]	[3Fe-4S]	[3Fe-4S]	[2Fe-2S]	[4Fe-4S]
P450 partner	CYP51	$P450_{SU1}$ (CYP105A1)	$P450_{SU1}$ (CYP105A1)	P450 cam (CYP101)	BioI (CYP107H1)
A_{max} [ϵ (mM^{-1} cm^{-1})]	412 (11.3)	410 (17.0)	410 (20.1)	321, 412 (11.0), 456	390 (ND)
EPR *g* value	2.03	2.03	2.02	2.02, 1.94	2.07, 1.93, 1.88
E_m (mV, vs SHE)	−31	ND	ND	−239/−196	−385

[a] The features of Mtb Fdx are compared with those for other [3Fe-4S] ferredoxins and ferredoxins with other types of iron−sulfur clusters involved in electron transfer to P450 enzymes. Fd1 and Fd2 are cognate ferredoxins for *St. griseolus* P450 enzymes (CYP105A1 and CYP105A2) involved in oxygenation of sulfonylurea herbicides (*74*). Putidaredoxin is the cognate ferredoxin for the *Ps. putida* camphor hydroxylase P450 cam (*25*). Fer is a viable ferredoxin partner for *B. subtilis* P450 BioI, involved in biotin synthesis (*41*). Maxima in the visible absorption spectra (A_{max}) are for the oxidized forms of the ferredoxins (*41*, *74*, *75*). The *g* value is for the EPR-active form of the iron−sulfur cluster in each case (reduced clusters in the case of putidaredoxin and *B. subtilis* Fer) (*41*, *72*, *76*). Redox potential data (where available) are relative to the standard hydrogen electrode (*41*, *77*). The values cited for putidaredoxin (Pd) are for free Pd/Pd bound to P450 cam. ND means not determined.

absorption in the reduced form, with a low-intensity absorption peak at 670 nm. There is an isosbestic point for the oxidized and reduced forms at 337 nm, and the reduced form has a peak at ~315 nm. Through spin quantitation by EPR (see below), extinction coefficients at peaks in the absorption spectrum for oxidized (reduced) forms of Fdx were determined: $\epsilon_{412} = 11\,300$ M^{-1} cm^{-1} (8150 M^{-1} cm^{-1}), $\epsilon_{315} = 15\,300$ M^{-1} cm^{-1} (18 300 M^{-1} cm^{-1}), and $\epsilon_{280} = 25\,300$ M^{-1} cm^{-1} (26 000 M^{-1} cm^{-1}) (Table 2). The far-UV CD spectrum of Fdx was typical of a protein with both helical and β-sheet structure. Minima were located at ~208 and 223 nm. Secondary structure prediction algorithms indicated approximately 39% α-helix and 24% β-sheet in Fdx (*38*).

Characterization of Mtb Fdx as a [3Fe-4S] Ferredoxin

Amino Acid Alignment. Three distinct types of iron−sulfur clusters are found in most forms of ferredoxin ([2Fe-2S], [3Fe-4S], and [4Fe-4S]). Bacterial P450 systems which exploit each of these different types have been characterized (*39*−*41*) (Table 2). The UV−visible spectrum of oxidized Fdx is distinct from that of typical [2Fe-2S] ferredoxins, which usually have more pronounced absorption features (e.g., ref *42*). In ferredoxins, iron atoms are coordinated by cysteines. The Fdx amino acid sequence is strongly similar to various [3Fe-4S] ferredoxins from other mycobacteria and actinomycetes (Figure 2B). There is a 66% level of amino acid sequence identity with the putative [3Fe-4S] ferredoxin from *Nocardiodes* spp. strain CF8, and a motif common to 3Fe-4S cluster-binding ferredoxins is shared between these proteins: Cys-X-X-X-X-X-Cys-X_n-Cys-Pro, where X is any amino acid and X_n indicates a number of variable amino acids around which iron ligands provided by the cysteine thiols are interspersed. In the [4Fe-4S] ferredoxins, the typical binding motif has a fourth cysteine in the position underlined in the [3Fe-4S] motif. Spectroscopic analyses were performed to characterize Fdx's iron−sulfur cluster.

EPR Analysis. EPR spectra of Mtb Fdx were recorded for oxidized and dithionite-reduced forms. Only oxidized Fdx displayed an EPR spectrum (Figure 3A). The oxidized Fdx EPR signal is typical of a $[3Fe\text{-}4S]^+$ cluster-containing protein, with a strong $g = 2.03$ resonance, characteristic of oxidized $[3Fe\text{-}4S]^+$ $S = {}^1/_2$ clusters (*43*) (Table 2). Integration of the EPR signal indicates that the cluster in this form accounts for >98% of the total protein, that is, having one spin per molecule (i.e., a single [3Fe-4S] cluster per protein molecule). The EPR signal was found to be virtually undetectable at temperatures of ≥30 K, again characteristic for a fast-relaxing $[3Fe\text{-}4S]^+$ cluster (*44*). Complete loss of the EPR signal occurred on reduction by dithionite, consistent with conversion of the EPR-active $[3Fe\text{-}4S]^+$ form to the

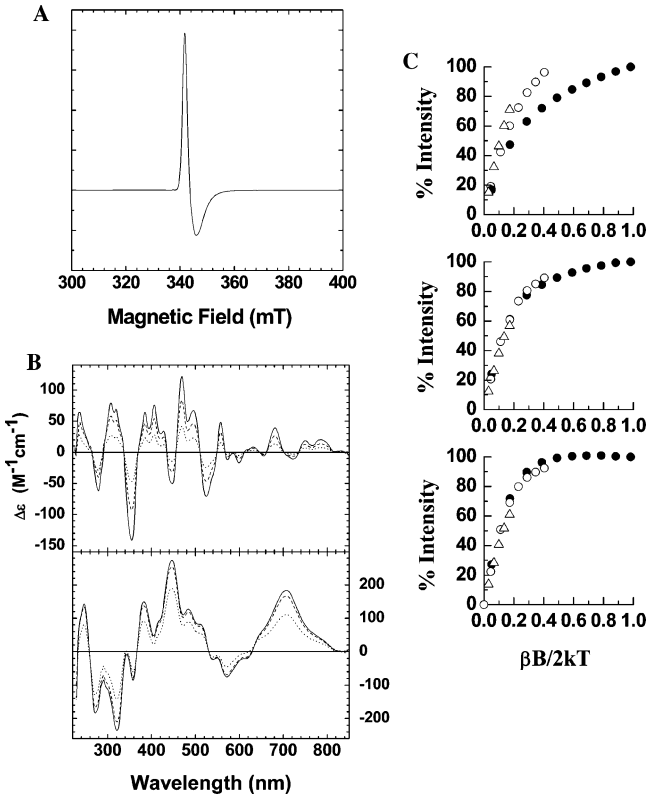

FIGURE 3: EPR and MCD spectroscopic analysis of Mtb Fdx. (A) An EPR spectrum of oxidized Mtb Fdx (800 μM) was recorded in 50 mM potassium phosphate (pH 7.5). No EPR signal was detectable for the dithionite-reduced species. Spectra were measured at 10 K with a power of 2 mW, a modulation amplitude of 2.1 G, and a microwave frequency of 9.68 GHz. The oxidized protein spectrum with a *g* of 2.03 indicates >98% of the protein sample contains a $[3Fe\text{-}4S]^+$ cluster. (B) Low-temperature MCD spectra (at 5 T) of oxidized (top panel) and dithionite-reduced (bottom panel) Fdx (270 μM) in 50 mM HEPES (pH 7.5). Spectra were recorded at 1.7 (solid line), 4.2 (dashed line), and 17 K (dotted line). (C) Magnetization curves for dithionite-reduced Fdx (270 μM) showing the percentage MCD signal intensity at 446 (top), 572 (middle), and 707.5 nm (bottom) at three different temperatures: 1.7 (●), 4.2 (○), and 10 K (△). The signal intensity is plotted vs the applied magnetic field expressed as $\beta B/2kT$, where β is the Bohr magneton, *B* is the applied field (tesla), *k* is Boltzmann's constant, and *T* is the absolute temperature (kelvin).

EPR-silent $[3Fe\text{-}4S]^0$ form. No conversion to a 4Fe-containing cluster was observed on reduction.

MCD Spectroscopy. To further analyze the Fdx iron−sulfur cluster, particularly with respect to characterization of the EPR-silent reduced form, we undertook magnetic circular dichroism (MCD) studies. MCD is diagnostic of spin and oxidation states of metal ions and is therefore a useful tool in the study of iron−sulfur clusters. MCD spectra vary significantly with cluster oxidation state, and unlike CD, MCD is relatively insensitive to the nature of the protein itself. Thus, MCD does not discriminate between structural differences in proteins, allowing direct characterization of the Fe−S cluster type and oxidation state in ferredoxins and other iron−sulfur proteins. MCD spectra of paramagnetic iron−sulfur proteins reveal the complexity of the electronic transitions that underlie the broad, rather featureless absorption spectra. These are diagnostic of the iron−sulfur cluster and oxidation state but, because of their complexity, cannot yet be interpreted in terms of fine differences in structure between similar cluster types. The MCD intensities of paramagnetic chromophores are inversely dependent on temperature and are generally $>10^2$ times more intense at 1.5 K than at 300 K (*45*). The low-temperature MCD spectra of the oxidized Fdx, $[3Fe\text{-}4S]^+$, were recorded at different temperatures and are shown in Figure 3B (top panel). The spectra demonstrate the temperature dependence features typical of a paramagnetic center, specifically an $S = {}^1/_2$ $[3Fe\text{-}4S]^+$ cluster, and are similar in shape and form to, for example, those of *Desulfovibrio gigas* ferredoxin II and the $[3Fe\text{-}4S]^+$ cluster form of mammalian aconitase (*46*).

The spectra of the reduced $[3Fe\text{-}4S]^0$ form of Fdx, shown in Figure 3B (bottom panel), are also similar to those of reduced $[4Fe\text{-}4S]^+$ clusters (e.g., ref *47*). However, these two types of iron−sulfur clusters can be distinguished by their signal intensity. Reduced Fdx displays MCD spectra of high intensity at the protein concentration that was used (270 μM), further confirming that the reduced cluster is the $[3Fe\text{-}4S]^0$ form. Typically, the intensity observed for $[4Fe\text{-}4S]^+$ clusters is >10-fold lower. In the reduced MCD spectra, the sharp peak of maximal intensity is at 446 nm, with other distinct features at 572 (trough) and 707.5 nm (peak).

To further differentiate between reduced $[3Fe\text{-}4S]^0$ ($S = 2$) and reduced $[4Fe\text{-}4S]^+$ ($S = {}^1/_2$) clusters, magnetization studies were carried out, examining the dependence of the MCD signal intensity on temperature and field strength. MCD measurements of reduced Fdx were performed at three different temperatures (1.7, 4.2, and 10 K), with variation of the applied magnetic field strength. Relationships between MCD signal intensity at 446, 572, and 707.5 nm and applied magnetic field are shown in Figure 3C (represented as a percentage of the maximal signal recorded at the relevant temperature and at 5 T, as shown in Figure 3B, bottom panel). Magnetization curves described at 446 nm are distinctly different at the three temperatures that were used. At 572 and 707.5 nm, the curves are relatively similar to one another but show a sharp increase in intensity with elevated field strength. The "nested" (not overlying) curves in panel A and the steep, bent curves in panels B and C are consistent with $S > {}^1/_2$ species and are not seen in $S = {}^1/_2$ species (such as $[3Fe\text{-}4S]^+$ or reduced $[4Fe\text{-}4S]^+$ clusters). These data provide further strong evidence that reduced Fdx has a $[3Fe\text{-}4S]^0$ $S = 2$ cluster, which is usually EPR-silent in perpendicular mode experiments. Hence, these results complement EPR studies and confirm that the Mtb Fdx has a single [3Fe-4S] cluster that cycles between the +1 and 0 oxidation states.

Spectroscopic Analysis of Mtb CYP51

Previous studies of the Fe(II)−CO state of CYP51 showed it to form predominantly P420 rather than the native P450 form, within a few minutes of binding the gaseous ligand. P420 is an inactive form in which thiolate ligation of the heme iron is lost, likely in favor of thiol ligation (i.e., through protonation of the proximal ligand) (*48*, *49*). Atomic structural data confirm Cys 394 as the proximal heme iron ligand. To establish native heme iron ligation in oxidized CYP51, we performed EPR on the ligand-free form. A typical rhombic EPR spectrum was obtained (at 10 K), with *g* values of 2.44, 2.25, and 1.91 (Table 1), similar to those reported previously (2.42, 2.26, and 1.91) (*37*) and to those we have reported for Mtb CYP121 (2.47, 2.25, and 1.90) (*22*, *28*). The values are also similar to those of *Saccharomyces cerevisiae* CYP51 (2.45, 2.27, and 1.92) and the CYP51 homologue from *Methylococcus capsulatus* (2.43, 2.26, and 1.91) (*50*, *51*). These *g* values are associated with a low-spin, hexacoordinated ferric heme iron with cysteinate and water as axial ligands. EPR spectra were also collected for ligand complexes of CYP51. When fluconazole binds (structural data indicate it coordinates directly to the heme via triazole nitrogen), the *g* values were not significantly altered from those of the ligand-free form (2.45, 2.26, and 1.90, compared with 2.45, 2.26, and 1.90 for fluconazole-bound CYP121). In the complex with 4-PIM (which also gives an inhibitory, type II spectral shift), an EPR spectrum similar to that described recently by Matsuura et al. (*37*) was obtained. The *g* values are as follows: $g_z = 2.53/2.47$, $g_y = 2.26$, and $g_x = 1.87$. The g_z component is the most resolved feature of the rhombic trio, and the two species present may be explained by the conformational heterogeneity of the protein or a freezing-induced effect. For example, these two spectral species could be explained by thiolate/imidazole ligation of the heme iron with imidazole in different conformations within the distal pocket. As discussed below, other evidence exists for conformational heterogeneity of Mtb CYP51. The EPR spectrum of the 2-PIM-bound form has major component *g* values of 2.42, 2.26, and 1.92, with a small proportion of the enzyme exhibiting the following values: $g_z = 2.47$ and $g_x = 1.90$. These are EPR signals characteristic of low-spin heme iron, and no evidence was found for high-spin signals, even in spectra re-recorded at lower temperatures and higher power. Thawed 2-PIM-bound CYP51 samples exhibited UV−visible spectra identical to those from prefreezing (with a large shoulder on the Soret band at ~392 nm) and suggested a substantially high-spin heme iron. Previous resonance Raman solution-state studies demonstrated that 2-PIM induced conversion of heme iron spin-state equilibrium toward five-coordinate high-spin (development of a ν_3 component at 1488 cm^{-1}) (*37*). Thus, the lack of a high-spin signal in EPR studies of 2-PIM-bound CYP51 suggests that there may be a thermal equilibrium between spin states (with negligible high-spin heme at low temperatures). Also as discussed below, solution-state UV−visible absorption studies suggest profound effects of tem-

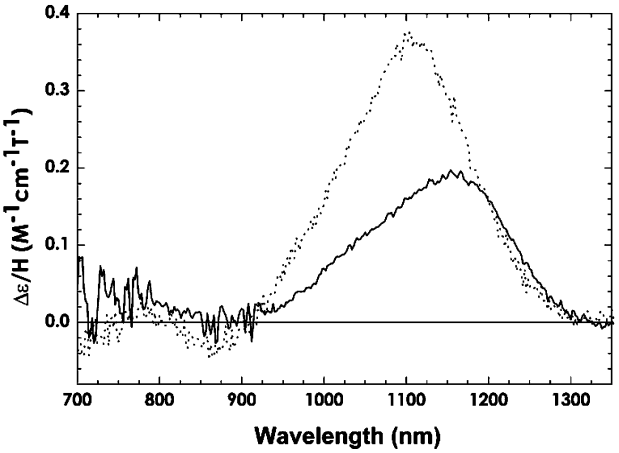

FIGURE 4: Room-temperature near-infrared MCD spectra of Mtb CYP51 and its fluconazole complex. The NIR region MCD spectra for wild-type ferric CYP51 (160 μM) in ligand-free and fluconazole-bound (200 μM) forms are shown as dotted and solid lines, respectively. The magnetic field was 6 T.

perature variation on heme iron spin-state equilibrium in the CYP51−2-PIM complex.

Resonance Raman studies of the oxidized, ligand-free form of CYP51 were also carried out at room temperature, with excitation at 406.7 nm, close to the Soret maximum. These data were again consistent with a low-spin, ferric resting state of the P450 at ambient temperature and similar to those reported previously using 413.1 nm excitation (*37*) (Table 1). The dominant oxidation-state marker (ν_4) is at 1372 cm^{-1}, the same frequency as for low-spin CYP121 (*22*) and confirmatory of the ferric state. The positions of CYP51 spin-state marker bands were also indicative of a predominantly low-spin heme iron. For instance, ν_3 is positioned at 1502 cm^{-1}, with only a very small shoulder at 1487 cm^{-1} (Table 1). The former indicates low-spin ferric heme, while the latter demonstrates only a very minor high-spin population. The situation is similar to that for CYP121 (ν_3 is split with the feature at 1500 cm^{-1} dominating over that at 1487 cm^{-1}) (*22*). By contrast, the lower-frequency component of ν_3 is predominant in *B. subtilis* P450 BioI, which is isolated in a mainly high-spin, fatty acid-bound form (*13*). Collectively, EPR and resonance Raman data indicate that oxidized, ligand-free CYP51 is a predominantly low-spin, thiolate-ligated enzyme. Thus, conversion to P420 is a consequence of reduction and/or binding of CO to the ferrous iron. This issue is explored further below.

Further analysis of CYP51 heme iron coordination was accomplished using MCD for the oxidized, ligand-free enzyme and the fluconazole complex. In the near-infrared region (~800−1400 nm), a charge transfer band for the low-spin P450 heme iron (CT_{LS}) can be diagnostic for the nature of the axial ligation of the heme iron (*47*). For ligand-free CYP51, the band is centered at 1110 nm, similar to that for CYP121 (1110 nm) and for *Bacillus megaterium* P450 BM3 (1080 nm), and consistent with thiolate and water ligation to the ferric iron (Figure 4) (*22*, *47*). For the fluconazole complex, the band shape and intensities throughout the spectrum are again consistent with a thiolate-ligated ferric heme iron. The band (lower in intensity than that for the ligand-free form) is at 1165 nm, similar to that for the imidazole complex of P450 BM3 (1180 nm), for cysteinate/histidine-ligated heme 2 of the thiosulfate oxidation enzyme SoxAX from *Rhodovulum sulfidophilum* (1150 nm), and for the proline/cysteine-ligated CooA (1190 nm) (*52*−*54*). The shift of the CT_{LS} band from ligand-free ferric to fluconazole-bound and the decrease in band intensity observed for CYP51 are almost identical to changes observed when fluconazole binds to CYP121 (1110 nm for the ferric, ligand-free form and 1160 nm for the fluconazole-bound form; H. E. Seward et al., unpublished results). The spectroscopic shifts on complexation with fluconazole are thus consistent with replacement of the aqua distal axial ligand with the azole, although the decrease in intensity is unexpected. Additionally, the EPR spectra of the fluconazole-bound form of CYP51 suggest coordination of fluconazole to the heme iron does not occur fully in frozen solution.

Potentiometric Analysis of Mtb CYP51 and Fdx

Previous studies of demethylation of dihydrolanosterol by CYP51 using either (i) *E. coli* flavodoxin reductase and flavodoxin or (ii) spinach ferredoxin and Mtb Fdx demonstrated that both systems exhibited similar efficiencies and that turnover was slow, requiring overnight incubation for demethylation of 20% of the substrate (*21*). To establish whether slow reactivity of the redox system might have its origin in the thermodynamic properties of Mtb Fdx and CYP51, we determined reduction potentials of the [3Fe-4S] and heme centers by spectroelectrochemistry. Potentials of the CYP51 heme iron were determined in the absence of substrate, when bound to lanosterol, and in the presence of 2-PIM and estriol, both of which induce a shift in the heme iron spin-state equilibrium toward the high-spin form. Previous studies on selected bacterial P450s have shown that substrate-induced changes in the spin-state equilibrium (resulting in a more positive reduction potential of the heme iron) trigger electron transfer to the heme iron from the redox partner and accelerate catalytic turnover (*55*, *56*).

Data for redox titration of substrate-free CYP51 are shown in Figure 5A. The spectrum for the oxidized enzyme has its Soret band at 419 nm with α and β bands at 572 and ~535 nm, respectively. On reduction, the Soret band loses intensity and shifts to ~423 nm. There are isosbestic points at ~405 and 430 nm. In the reduced form, features develop at 558.5 and 530 nm, with the former being higher in intensity. Fitting of absorption (at 419 nm) versus potential data to the Nernst equation (Figure 5A, inset) produces a heme iron midpoint potential of -375 ± 5 mV (against the standard hydrogen electrode). The heme iron potential is in a range similar to that observed for other bacterial P450s. For example, substrate-free P450 BM3 has a potential of -427 ± 4 mV, while substrate-free P450 cam has a potential of approximately −300 mV (*56*, *57*) (Table 1). However, the nature of the optical change that occurs for CYP51 on reduction is distinct from that seen in these other enzymes. Rather than a Soret shift to a shorter wavelength on reduction (~410 nm), the CYP51 Soret band moves to a longer wavelength. Moreover, spectral changes seen in the Q-band region are also distinctive, particularly with respect to the increased intensity at 558.5 nm. The observed spectral changes are similar to those seen for the H93G variant of sperm whale myoglobin, for which cyclopentanethiol and tetrahydrothiophene sulfur donors were used to generate thiol-ligated ferrous forms (*58*). Thus, spectral changes for ferrous CYP51 appear to be consistent with protonation of

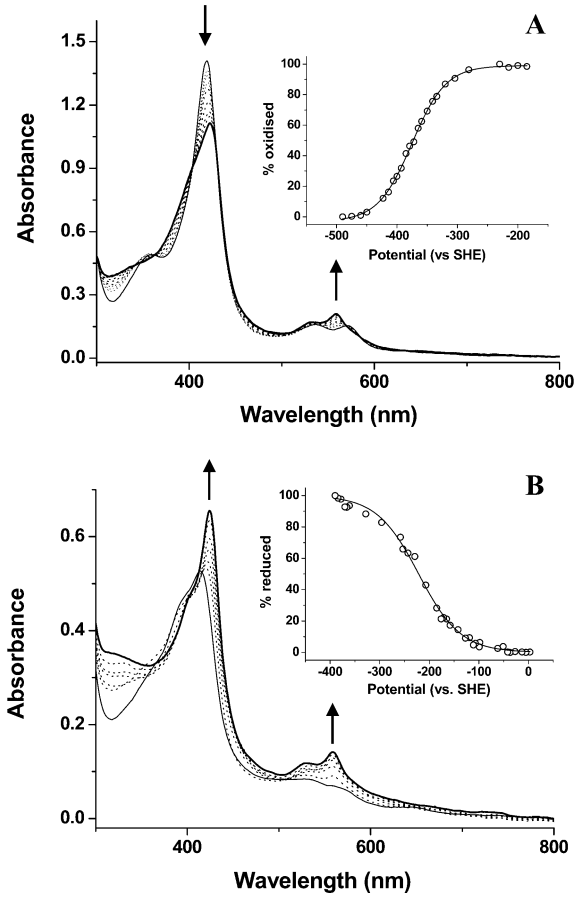

FIGURE 5: Potentiometric analysis of Mtb CYP51 in ligand-free and estriol-bound forms. (A) Spectral changes associated with reductive titration of ligand-free CYP51 (10.1 μM). The spectrum for the oxidized enzyme (Soret maximum at 419 nm) is shown as a thin solid line. The reduced enzyme at the end point of the titration is shown as a thick solid line (Soret maximum at 423 nm). Selected spectra recorded at intermediate points in the titration are shown as dotted lines. The inset shows a fit of absorption (at 419 nm) against applied potential, with data fitted to the Nernst equation. The potential of the ligand-free CYP51 heme iron was determined to be -375 ± 5 mV. (B) Spectral changes associated with reductive titration of CYP51 (6.3 μM) in the presence of 90 μM estriol. Oxidized, intermediate, and reduced spectra are again shown as thin solid, dotted, and thick solid lines, respectively. The inset shows a fit of absorption (at 423 nm) against applied potential, with data fitted to the Nernst equation. The potential of the estriol-bound CYP51 heme iron was determined to be -225 ± 10 mV.

the thiolate ligand (Cys 394) to a thiol, a transition that likely underlies conversion of P450 to the inactivated P420 form. As discussed further below, CYP51 undergoes rapid conversion of the Fe(II)−CO complex from P450 to P420, probably as a result of protonation of the Cys 394 thiolate.

For estriol-bound CYP51, similar spectral changes occur on heme ion reduction (Figure 5B). In the estriol-bound form, the oxidized spectrum is that of a mixed-spin heme (low- and high-spin components) and the Soret is lower in intensity than that for the reduced form (which has an A_{max} at ~424 nm). In the Q-band region, substantial increases in band intensity are seen, with peaks at 558.5 and 530 nm, as in the ligand-free form. The inset shows the fit of absorption (424 nm) versus potential, generating a midpoint potential of -225 ± 8 mV. Thus, estriol binding results in a substantial increase in CYP51 heme iron potential, favoring heme iron reduction. Increases similar in magnitude are observed for

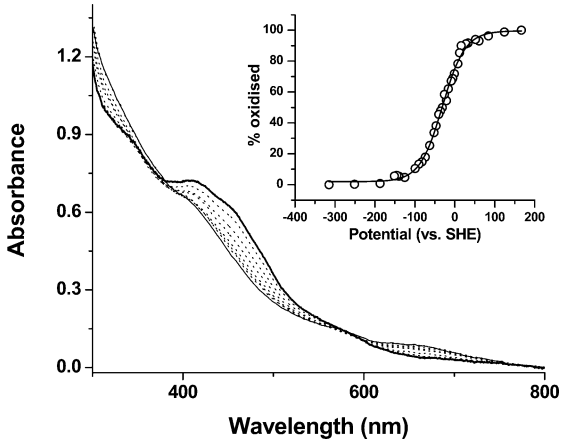

FIGURE 6: Potentiometric titration of Mtb Fdx. Spectral changes associated with the reductive titration of Mtb Fdx are shown. For clarity, only selected spectra are shown. The bold solid line is that of the fully oxidized Fdx (63 μM) recorded at a potential of 94 mV (vs the standard hydrogen electrode). The thin solid line is that for the fully reduced Fdx (recorded at −313 mV). Dotted lines are selected spectra recorded at intermediate potentials. The inset shows a fit of absorption (at 480 nm, near the wavelength of maximal overall absorption change between oxidized and reduced forms) against applied potential, with data fitted to the Nernst equation. The potential for the Fdx $[3Fe\text{-}4S]^{+}$-to-$[3Fe\text{-}4S]^{0}$ transition was determined to be -31 ± 5 mV.

both P450 cam and P450 BM3 (*55*, *56*). For 2-PIM-bound CYP51, spectral changes observed on heme iron reduction are broadly similar to those for estriol-bound CYP51, but the data are poorer in quality due to gradual precipitation of the ligand [which is at a high concentration (7.5 mM) due to its low affinity for CYP51] and concomitant protein aggregation during the course of the redox titration. Notwithstanding these problems, a midpoint heme iron reduction potential of -220 ± 20 mV (similar to that for the estriol-bound form) was determined for 2-PIM-bound CYP51 from data fitting of absorption change versus potential data at the Soret peak.

Spectral changes accompanying reduction of Fdx are shown in Figure 6, with the fit of absorption versus potential data to the Nernst equation shown as the inset. The reduction potential for the $[3Fe\text{-}4S]^{+}$-to-$[3Fe\text{-}4S]^{0}$ transition is -31 ± 5 mV (Table 2), substantially more positive than that of the substrate-free CYP51. The potential of Fdx was redetermined in its complex with CYP51. The potential was not significantly altered (-33 ± 4 mV), and the potential of the CYP51 heme iron was similarly unaffected (-370 ± 4 mV). Thus, despite the fact that Fdx has been shown to support turnover of CYP51 (with spinach ferredoxin reductase as the electron donor to Fdx), there is an apparent thermodynamic barrier to Fdx-dependent reduction of the CYP51 heme iron. For both CYP51 and Fdx, the redox titrations were fully reversible. No hysteretic behavior was observed, and the spectra recorded in oxidative and reductive directions were nearly identical at the same applied potentials.

Instability of the CYP51 Ferrous−Carbon Monoxy Complex

The ferrous (dithionite-reduced) CYP51 binds CO avidly, which is characteristic of P450s. However, the native complex (Soret at 448.5 nm) is unstable and collapses over several minutes to form the inactive P420 species (refs *21*

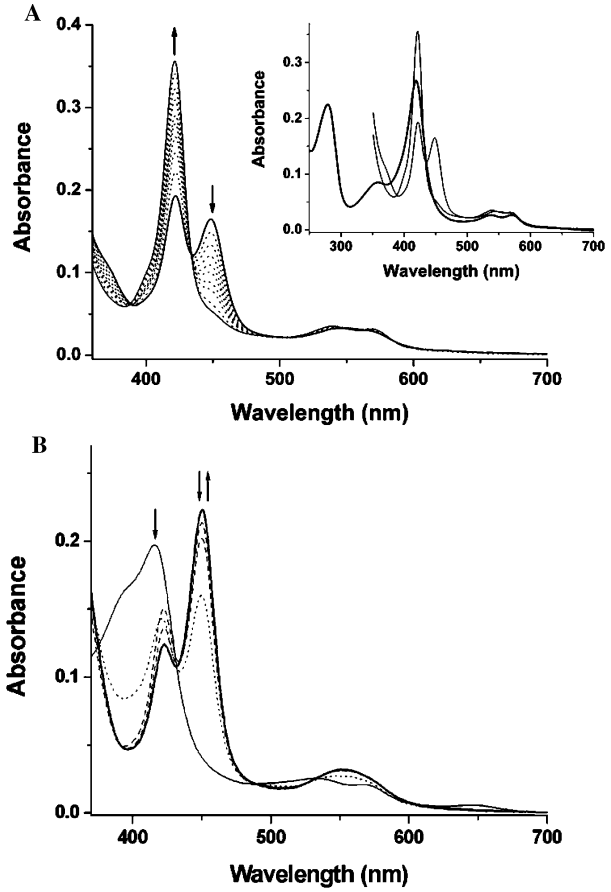

FIGURE 7: Collapse of the CYP51 ferrous−carbon monoxy complex from P450 to P420 and stabilization by estriol. (A) The main panel shows absorption changes occurring during collapse of the reduced, CO-bound form of substrate-free CYP51 (1.94 μM) from the P450 form to the P420 form. The spectrum shown as a bold, solid line (with the greatest absorption at 448.5 nm) was that collected 2 min after addition of CO to the reduced enzyme sample and is the spectrum with the largest P450 content. Subsequent spectra (dotted lines recorded 2.5, 3.5, 4, 4.5, 5.5, 6.5, and 14.5 min after CO addition) show the progressive decay of the P450 form in favor of the P420 form, with the maximal Soret absorption at 421.5 nm. The final spectrum (thin, solid line) was recorded at 32.5 min and shows complete conversion to P420. Arrows indicate the directions of absorption change. The inset shows the spectrum of oxidized CYP51 (thick, solid line) alongside those spectra exhibiting maximal P450 and maximal P420 content (thin, solid lines). The intensity of the Soret band in the P420 species is substantially greater than in the oxidized CYP51. (B) A similar data set for the estriol-bound form of CYP51 (1.98 μM). In this case, the P450 species is dramatically stabilized. The spectrum for the oxidized enzyme is shown as a thin, solid line. The dotted line is that for the reduced CYP51 1.5 min after addition of CO. The thick, solid line (maximal P450 content) was recorded 3.5 min after CO addition. Dashed lines with decreasing P450 intensity were recorded 9.5 and 34 min following CO addition. Arrows indicate the directions of absorption change during the reactions.

and *48* and Figure 7A). The final species has its Soret maximum at 421.5 nm and an isosbestic point for the transition at ~434 nm. The instability of the P450 form is not related to the nature of the reductant, since collapse to P420 occurs over a similar time period regardless of whether the electron for ferric heme iron reduction is supplied by an artificial reductant (dithionite) or by NAD(P)H via redox partner enzymes [either *E. coli* flavodoxin reductase and flavodoxin (*59*) or the Mtb FprA and Fdx proteins (*27*)]. At pH 7.0, the rate of P420 formation (from the progress curve of ΔA_{420} vs time) is a monoexponential process with a rate constant of 0.246 ± 0.007 min^{-1}. The rate is not markedly changed in the pH range between 6.5 and 8.5 but is accelerated to 0.298 ± 0.019 min^{-1} at pH 6.0. As expected from previous results, the rate of P420 formation in dithionite-reduced CYP51 was also not affected by complexation with Mtb Fdx. In recent studies, Ortiz de Montellano and co-workers demonstrated conversion of the P420 form of *Sorangium cellulosum* P450 epoK (involved in the synthesis of epothilones, potential anticancer agents) to the P450 form in the presence of the substrate epothilone D (*60*). By contrast, addition of estriol or 2-PIM to the Mtb CYP51 P420 species failed to induce any significant degree of reconversion to the P450 form, even at a low temperature (15 °C) or in the presence of 10% glycerol (as done for the epoK P450). However, formation of CYP51 P420 is clearly not irreversible. Following complete aerobic reoxidation of the P420 complex, the spectrum returns to that characteristic of the resting ferric, ligand-free form. Re-reduction of this sample in the presence of CO results in formation of a considerable amount of P450 complex (A_{max} = 448.5 nm, ~40% recovery), which subsequently decays completely to P420 again at a rate similar to that previously observed.

Despite estriol's apparent inability to reconvert P420 to P450, binding of the sterol did result in a considerable retardation of the rate of P420 formation. As seen in Figure 7B, a substantially greater amount of P450 is formed following reduction and addition of CO to the estriol-bound form. The decay to P420 occurs with an apparent rate of 0.062 ± 0.004 min^{-1}. Binding of 2-PIM had a small effect on the P450 collapse, with kinetic analysis indicating a decrease in the rate of P420 formation to 0.219 ± 0.006 min^{-1}.

Kinetics of Interactions between CYP51 and Fdx

Stopped-Flow Analysis. The rate of Fdx-dependent reduction of CYP51 heme iron was measured by following formation of the CO complex (at 448 nm) as described in Experimental Procedures. In the absence of ligand, a rate (k_{red}) of 3.0 ± 0.1 min^{-1} was determined for the electron transfer reaction. In presence of estriol, the rate was slightly faster ($k_{red} = 4.3 \pm 0.1$ min^{-1}), but the rate in the presence of 2-PIM was not significantly different from that of the ligand-free enzyme ($k_{red} = 3.0 \pm 0.1$ min^{-1}). These rates are ~14−65-fold faster than those of the P450-to-P420 collapse measured under similar conditions (see the previous section). Despite the thermodynamically favorable shift in heme iron reduction potential in the presence of these ligands, a small increase in the electron transfer rate was observed only for estriol-bound CYP51. The collapse of the P450 form to P420 occurred on a longer time scale, and the rate of this conversion (k_{conv}) was determined from the same data set using global analysis software. In the absence of ligand, the rate of P420 formation was ~10-fold slower than that of P450 formation in the presence of Fdx ($k_{conv} = 0.294 \pm 0.008$ min^{-1}). There was a small degree of stabilization of the P450 form in the presence of 2-PIM ($k_{conv} = 0.174 \pm 0.009$ min^{-1}) but a substantial stabilization in the estriol-bound form ($k_{conv} = 0.018 \pm 0.001$ min^{-1}) as observed also in spectroscopic studies. Thus, despite their similar abilities to induce formation of high-spin heme iron in CYP51, 2-PIM and estriol differ considerably in their abilities to stabilize the P450 (i.e.,

thiolate-ligated) form of CYP51. The bulky estriol (which likely mimics more closely CYP51's natural substrate) is far more effective than the much smaller 2-PIM molecule. Possibly, the slower P420 collapse rates estimated in the Fdx-driven system for the estriol-bound form (cf. rates for the dithionite-reduced form) reflect some further stabilization of P450 mediated by Fdx−CYP51 interactions.

Steady-State Analysis. To analyze the affinity of CYP51 for Fdx and to investigate whether 2-PIM or estriol binding accelerates NADPH-dependent electron transfer activity in a Mtb class I redox system comprised of FprA, Fdx, and CYP51, steady-state kinetic studies were performed as described in Experimental Procedures. In the absence of an exogenous ligand, the rate of NADPH oxidation (k_{cat}) was 0.81 ± 0.02 min^{-1} and the apparent K_d for the interaction between CYP51 and Fdx was 30.7 ± 0.7 μM. In the presence of 2-PIM, these values were 1.36 ± 0.09 min^{-1} and 27.3 ± 1.2 μM, respectively, and in the estriol-bound form, the parameters were 1.89 ± 0.13 min^{-1} and 24.3 ± 1.0 μM, respectively. Thus, the apparent binding constant for Fdx is relatively constant regardless of the presence of ligands, and there is a k_{cat} increase of up to ~2.3-fold in the presence of estriol. The kinetic values are consistent with Fdx-to-CYP51 electron transfer as a major rate-limiting step in each of the steady-state reactions (see the preceding section).

Thermal Effects on the CYP51 Heme Iron Spin-State Equilibrium

Previous studies on P450 cam demonstrated temperature-dependent changes in the optical spectrum of the substrate-bound and substrate-free forms of the enzyme, reflecting increased high-spin heme content as the incubation temperature is elevated (*56*). Similar results were obtained with P450 BM3 (A. W. Munro et al., unpublished data). In view of the unusual absence of high-spin heme iron in the EPR samples of the CYP51−2-PIM complex (despite clear evidence for high-spin heme iron content from optical titrations; see Figure 1B), we examined changes in the spectral properties of the ligand-free form and 2-PIM- and estriol-bound forms of CYP51 across the temperature range of 5−50 °C. Above 50 °C, excessive protein aggregation and precipitation occurred, but within the working range, distinctive changes in optical spectra were observed for the three species. Ligand-free CYP51 exhibited small decreases in A_{419} and increased absorption at ~390 nm as the temperature was increased, consistent with an elevated high-spin heme iron content. Estriol-bound CYP51 behaved similarly, displaying changes slightly greater in amplitude. However, the 2-PIM-bound form displayed the opposite behavior, with an apparent decrease in high-spin content with elevation of temperature and with an isosbestic point close to 410 nm (Figure 8). The result was replicated in phosphate buffer, indicating that the effect was not related to subtle pH changes in the buffer. Since 2-PIM was present in a large excess, the phenomenon cannot be readily explained by temperature-dependent changes in K_d for 2-PIM. This unusual behavior may reflect a temperature-dependent change in the protein conformational state or 2-PIM binding mode. Such thermally induced structural alterations might also underlie an apparent absence of a high-spin heme iron signal in the EPR experiments detailed above. In P450 cam, the 2-PIM complex (from atomic structural studies) occurs

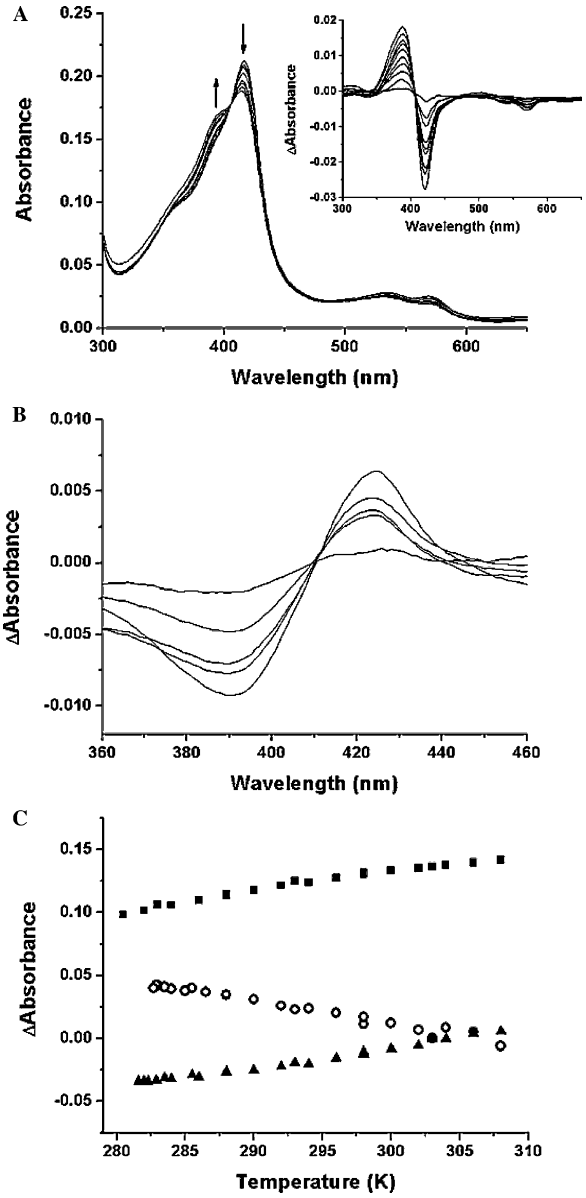

FIGURE 8: Thermal effects on optical properties of CYP51 bound to estriol and to 2-PIM. (A) The main panel shows absolute spectra for estriol-bound CYP51 (1.57 μM) at various temperatures. The spectrum with the highest Soret intensity at 419 nm was recorded at 279 K. Subsequent spectra were recorded at progressively higher temperatures (282, 284, 288, 296, 298, 304, and 310 K) and show progressive decreases in absorption at 419 nm (low-spin heme iron) with development of absorption at 394 nm (high-spin form). An isosbestic point is located at 405 nm. Arrows indicate the directions of absorption change with an increase in temperature. The inset shows difference spectra from the thermal titration of estriol-bound CYP51 (generated by subtraction of the absolute spectrum recorded at 279 K from spectra recorded at higher temperatures). Spectra of increasing intensity were recorded at 280.5, 283, 286, 290, 292, 293, 298, 300, 302, and 308 K. (B) Difference spectra for 2-PIM-bound CYP51 (0.84 μM) at various temperatures. The spectral conversion with an increasing temperature is the opposite of that observed for ligand-free or estriol-bound CYP51 and is indicative of an increasing low-spin heme iron component at higher temperatures. Spectra (with progressive increases in intensity) were recorded at 286, 298, 302, 304, and 314 K. (C) Maximal temperature-induced absorption change in the Soret region [$A_{390} - A_{425}$ for the 2-PIM-bound form (○), $A_{389} - A_{423}$ for the estriol-bound form (■), and $A_{388} - A_{422}$ for the ligand-free CYP51 (▲)], as described in Experimental Procedures. Data are shown in the range from 280 to 310 K. Spectral perturbations due to protein aggregation were observable at ≥315 K.

with the ligand benzene ring oriented toward the heme iron and the distal water ligand maintained (*61*). It appears likely that this type of ligand binding mode is also favored in CYP51 as the temperature is increased.

DISCUSSION

P420 formation in CYP enzymes can be induced by, for example, treatment with denaturants (e.g., ref *62*) or application of high hydrostatic pressure (e.g., ref *63*). However, spontaneous conversion of the CYP51 P450 complex to P420 is relatively unusual. The electronic transition that characterizes the P450 form arises from proximal heme iron coordination by a cysteinate (Cys 394 in Mtb CYP51). The P420 form is considered to result from loss of thiolate coordination and, specifically, from the protonation of the ligand to a thiol (*59*). Thus, we consider that time-dependent conversion of the P450 form of Mtb CYP51 to P420 reflects continuous protonation of the thiolate ligand until the transition is complete. The fact that anaerobic equilibrium titrations with dithionite (in the absence of CO) produce a ferrous CYP51 species in which the Soret maximum is red-shifted (A_{max} = 421.5 nm) with respect to that for the ferric form (419 nm) suggests that thiolate protonation may occur as a consequence of iron reduction regardless of CO ligation. The ligand α-naphthoflavone was shown to stabilize the P450 form of *E. coli*-expressed CYP4B1 and CYP1A2 during purification (*64*). However, in these cases, whether reductive inactivation with thiolate protonation was responsible for P420 formation in absence of ligand or whether the bound ligand produced some other structural effect to maintain thiolate coordination was not demonstrated. EPR and MCD spectroscopic analysis demonstrate that thiolate ligation is in place for the oxidized CYP51 but that reduction (whether protein-mediated or using dithionite) results in a spectral conversion similar to that observed for thiol-coordinated myoglobin and thus likely indicates redox-induced protonation of the CYP51 Cys 394 thiolate. Other well-characterized bacterial P450s produce blue-shifted Soret transitions on heme iron reduction (e.g., from 419 to 410 nm for P450 BM3 and from 416.5 to 405 nm for Mtb CYP121), while CYP51 exhibits a Soret red shift on reduction. Other optical changes in the Q-band region (including elevated absorption at 558.5 nm, as opposed to the loss of resolution of the Q-bands as seen for, e.g., ferrous P450 BM3) are also strongly indicative of development of thiol coordination in ferrous CYP51, as seen for the thiol-coordinated myoglobin variant (*59*). Thus, ferrous, ligand-free CYP51 is unstable and undergoes a switch from thiolate to thiol coordination in the proximal ligand position.

In recent work, Ortiz de Montellano's group demonstrated substrate (epothilone D)-dependent reconversion of P420 to P450 in P450 epoK. This was likely due to protection of the enzyme from structural perturbations associated with heme iron reduction that resulted in protonation of the heme cysteinate ligand (*60*). In the epoK system, fatty acids (which also bind close to the heme) fail to stabilize the P450 form, suggesting that the effect is specific to "true" substrate or substrate-like structures. No kinetic analysis was presented for P420 formation in the epoK system. With ligand-free CYP51, we show here that the collapse of P450 to P420 occurs with a rate of 0.246 min^{-1} at pH 7.0 and that binding of 2-PIM has, at best, a small stabilizing effect on the P450 form (0.219 min^{-1}). Estriol considerably stabilizes the P450 form, with the collapse rate decreased to $\leq$0.062 min^{-1}. However, even in the estriol-bound form, the equilibrium for the ferrous enzyme lies in favor of the thiol-ligated form, as seen both in the presence of CO by the P450-to-P420 transition and from spectral changes observed in absence of CO during potentiometric titrations. The difference in the P420−P450 equilibrium in CYP51 and P450 epoK may be related to the fact that epothilone D binds more tightly to P450 epoK (K_m = 1.6 μM) than estriol binds to CYP51 (K_d = 21.7 μM), to the lower solubility of the sterol, and/or to differences in the rate of thiolate protonation in the two P450s. Estriol is unlikely to be a true physiological substrate for Mtb CYP51, and it is thus quite feasible that a tighter binding substrate might facilitate reconversion of P420 CYP51 to the P450 form. However, it should be noted that a substantial proportion of fully reoxidized P420 CYP51 can be reconverted to the P450 CO complex (which then collapses again to P420), indicating that thiol ligand deprotonation is reversible and occurs readily in the ferric CYP51. It is probable that such stabilization of active, thiolate-ligated heme iron by physiologically relevant substrates is a common property of the P450s. In recent studies, a similar P450-to-P420 collapse was observed for the enzyme prostacyclin cyclase. In this case, the collapse was more rapid (∼42 min^{-1} under the conditions that were examined), although effects of bound substrate on this process were not examined. Complete reoxidation of the P420 complex (with CO dissociation) resulted in the formation of a species with native-like Soret absorption character and ∼50% of the activity of the starting form. However, the ability of the reoxidized species to re-form the CO-bound, thiolate-coordinated P450 state was not demonstrated (*65*).

A further unusual feature of CYP51 is the difference in binding of various phenylimidazoles. Both 1-PIM and 4-PIM are typical heme-coordinating type II inhibitors (albeit with markedly different K_d values), but 2-PIM fails to ligate the heme iron and instead binds relatively weakly to CYP51 and induces a spin-state shift in the heme iron toward the high-spin form (K_d = 3.19 ± 0.37 mM). 2-PIM also exhibits unusual properties with respect to the temperature dependence of the CYP51 heme iron spin-state equilibrium. Elevated temperatures produce increased high-spin heme iron content for both ligand-free and estriol-bound forms but an opposite effect for 2-PIM-bound CYP51. Control experiments and the high concentration of 2-PIM used in these experiments indicate that this phenomenon is unrelated to thermally induced changes in buffer pH or to dissociation of 2-PIM. Instead, it may reflect alterations in the 2-PIM binding mode in the active site or other structural rearrangements in the ligand-bound form. EPR studies reported here and previously (at either 10 or 15 K) reveal only a very small amount of high-spin heme iron present in 2-PIM-bound CYP51. Despite this, both UV−visible absorption spectroscopy and resonance Raman data demonstrate substantial high-spin content at ambient temperatures (*37*). It appears that, at physiologically relevant temperatures, 2-PIM binds close to the aqua ligand to the heme iron and causes its displacement. However, steric or other constraints prevent direct coordination of the imidazole group to the CYP51 heme iron, and instead, a type I optical change is produced. Structural analysis of the 2-PIM complex of P450 cam showed that the ligand bound with its benzene ring oriented

toward the heme iron, and the distal water was retained on the heme iron in a low-spin complex (*61*). Spectroscopic analysis of the 2-PIM complex with human endothelial eNOS also revealed a binding mode that did not involve imidazole coordination of the heme iron. In this case, a high-spin heme iron complex was formed, as with Mtb CYP51 (*66*). The unusual temperature dependence of the spin state in the CYP51−2-PIM complex suggests that the equilibrium position of the ligand changes with temperature such that a P450 cam-like complex (i.e., with water restored as the axial ligand) is more highly populated with an increase in temperature.

In this paper, we present the first detailed characterization of the Mtb ferredoxin Fdx, the gene for which (*Rv0763c*) is located immediately upstream of CYP51 (*12*). It is likely that the two genes are cotranscribed and that they are physiological redox partners. Of the 20 P450s on the genome, only CYP51 and CYP143 are located adjacent to ferredoxins. CYP143 (encoded by the *Rv1785c* gene) and the ferredoxin product of *Rv1786* (a putative [3Fe-4S] ferredoxin) are encoded by genes that are divergently transcribed on different DNA strands. Studies presented in this paper and previously published data demonstrate that electron transfer occurs in a Fdx−CYP51 complex and that sterol demethylation occurs when the proteins are reconstituted with NADPH and a ferredoxin reductase (*21*). Detailed spectroscopic studies carried out here, including analysis of (i) the temperature dependence of the EPR signal for oxidized Fdx and (ii) the MCD of reduced Fdx and magnetization effects on MCD of reduced Fdx, clearly demonstrate that Fdx is a [3Fe-4S] ferredoxin, and the presence of any significant amount of [4Fe-4S] cluster is ruled out. Accurate determinations of extinction coefficients for Fdx are made on the basis of a combination of EPR and optical studies.

Potentiometric analysis indicates that the reduction potential of the iron−sulfur cluster in Fdx is −31 mV, considerably more positive than that for ligand-free CYP51 (−375 mV). The reduction potential for estriol-bound CYP51 is much more positive (−225 mV). Despite the apparent thermodynamic barrier to electron transfer, Fdx can clearly reduce CYP51 and sterol substrates were demethylated in a NADPH-dependent manner using a plant ferredoxin reductase to mediate electron transfer from NADPH ($E_m = -320$ mV) to Fdx. Activity levels are similar to those observed with the *E. coli* flavodoxin reductase and flavodoxin as redox partners (*21*). There is a positive driving force (of ∼95 mV) for electron transfer from NADPH through the redox chain (FprA and Fdx) to CYP51. Thus, the overall process is thermodynamically favorable, and the intermediate Fdx-to-P450 step may be a regulatory step that controls the overall rate. Binding of dioxygen to ferrous CYP51 heme iron likely prevents reverse electron transfer and favors delivery of the second electron to a ferrous−oxy substrate-bound P450 complex. Arguably, the slow-growing Mtb pathogen (which remains dormant for extended periods in the host) has evolved a thermodynamic barrier for electron transport from Fdx to CYP51 as a mechanism for downregulating CYP51 activity, possibly to avoid overaccumulation of products. However, it is not clear whether sterols are physiological substrates for Mtb CYP51. These compounds are not endogenously produced in Mtb, although host cholesterol is essential for Mtb infectivity (*67*). Possibly, sterol demethylation is an evolutionary "relic" activity of a P450 that now has a distinct role in Mtb physiology. As with other P450 systems in Mtb, the physiological role of CYP51 remains to be elucidated.

In conclusion, we present a detailed characterization of thermodynamic and spectroscopic properties of the Mtb ferredoxin Fdx and its cognate P450 CYP51. Kinetics of electron transfer reactions between the enzymes are characterized for the first time, and the first viable Mtb P450 class I redox chain is reconstituted using Fdx, CYP51, and the ferredoxin reductase FprA. These studies demonstrate that protonation of the cysteinate ligand to the ferrous CYP51 underlies the collapse of the Fe(II)−CO adduct of the enzyme from its P450 to its P420 form and also show clearly that the protonation is reversible and that the rate of P420 formation is substantially retarded in the estriol-bound form of CYP51. Non-standard thermal effects on CYP51 heme iron spin-state changes are observed in the 2-PIM-bound enzyme, consistent with the structural plasticity of CYP51 and/or temperature-dependent ligand binding modes. This, in turn, is consistent with recent structural data on Mtb CYP51, which highlight the importance of conformational flexibility in the protein and suggest that conformational changes expose alternative entry and exit ports for substrate(s) and product(s) (*24*). Collectively, these studies detail novel features of the only structurally characterized member of one of the evolutionarily oldest and most widely conserved P450 families.

REFERENCES

1. Cole, S. T. (2002) Comparative and functional genomics of the *Mycobacterium tuberculosis* complex, *Microbiology 148*, 2919−2928.
2. Domenech, P., Barry, C. E., III, and Cole, S. T. (2001) *Mycobacterium tuberculosis* in the post-genomic age, *Curr. Opin. Microbiol. 4*, 28−34.
3. Duncan, K., and Barry, C. E., III (2004) Prospects for new antitubercular drugs, *Curr. Opin. Microbiol. 7*, 460−465.
4. Saint-Joanis, B., Souchon, H., Wilming, M., Johnsson, K., Alzari, P. M., and Cole, S. T. (1999) Use of site-directed mutagenesis to probe the structure, function and isoniazid activation of the catalase/peroxidase, KatG, from *Mycobacterium tuberculosis*, *Biochem. J. 338*, 735−760.
5. Frieden, T. R., Sterling, T. R., Munsiff, S. S., Watt, C. J., and Dye, C. (2003) Tuberculosis, *Lancet 362*, 887−899.
6. Davies, P. D. (2003) The role of DOTS in tuberculosis treatment and control, *Am. J. Respir. Med. 2*, 203−209.
7. Desta, Z., Soukhova, N. V., and Flockhart, D. A. (2001) Inhibition of cytochrome P450 (CYP450) isoforms by isoniazid: Potent inhibition of CYP2C19 and CYP3A, *Antimicrob. Agents Chemother. 45*, 382−392.
8. De Barber, A. E., Mdluli, K., Bosman, M., Bekker, L. G., and Barry, C. E., III (2000) Ethionamide activation and sensitivity in multidrug-resistant *Mycobacterium tuberculosis*, *Proc. Natl. Acad. Sci. U.S.A. 97*, 9677−9682.
9. Pym, A. S., Saint-Joanis, B., and Cole, S. T. (2002) Effect of katG mutations on the virulence of *Mycobacterium tuberculosis* and the implication for transmission in humans, *Infect. Immun. 70*, 4955−4960.
10. Cole, S. T., Brosch, R., Parkhill, J., Garnier, T., Churcher, C., et al. (1998) Deciphering the biology of *Mycobacterium tuberculosis* from the complete genome sequence, *Nature 393*, 537−544.
11. Cole, S. T. (1999) Learning from the genome sequence of *Mycobacterium tuberculosis* H37Rv, *FEBS Lett. 452*, 7−10.
12. Gunsalus, I. C., and Wagner, G. C. (1978) Bacterial P-450cam methylene monooxygenase components: Cytochrome m, putidaredoxin, and putidaredoxin reductase, *Methods Enzymol. 52*, 166−188.
13. Lawson, R. J., Leys, D., Sutcliffe, M. J., Kemp, C. A., Cheesman, M. R., Smith, S. J., Clarkson, J., Smith, W. E., Haq, I., Perkins,

J. B., and Munro, A. W. (2004) Thermodynamic and biophysical characterization of cytochrome P450 BioI from *Bacillus subtilis*, *Biochemistry 43*, 12410−12426.

14. Green, A. J., Rivers, S. L., Cheesman, M. R., Reid, G. A., Quaroni, L. G., Macdonald, I. D., Chapman, S. K., and Munro, A. W. (2001) Expression, purification and characterization of cytochrome P450 BioI: A novel P450 involved in biotin synthesis in *Bacillus subtilis*, *J. Biol. Inorg. Chem. 6*, 523−533.
15. Lee, D. S., Yamada, A., Sugimoto, H., Matsunaga, I., Ogura, H., Ichihara, K., Adachi, S., Park, S. Y., and Shiro, Y. (2003) Substrate recognition and molecular mechanism of fatty acid hydroxylation by cytochrome P450 from *Bacillus subtilis*: Crystallographic, spectroscopic, and mutational studies, *J. Biol. Chem. 278*, 9761−9767.
16. Gustafsson, M. C., Roitel, O., Marshall, K. R., Noble, M. A., Chapman, S. K., Pessegueiro, A., Fulco, A. J., Cheesman, M. R., von Wachenfeldt, C., and Munro, A. W. (2004) Expression, purification, and characterization of *Bacillus* subtilis cytochromes P450 CYP102A2 and CYP102A3: Flavocytochrome homologues of P450 BM3 from *Bacillus megaterium*, *Biochemistry 43*, 5474−5787.
17. McLean, K. J., Marshall, K. R., Richmond, A., Hunter, I. S., Fowler, K., Kieser, T., Gurcha, S. S., Besra, G. S., and Munro, A. W. (2002) Azole antifungals are potent inhibitors of cytochrome P450 mono-oxygenases and bacterial growth in mycobacteria and streptomycetes, *Microbiology 148*, 2937−2949.
18. Podust, L. M., Kim, Y., Arase, M., Neely, B. A., Beck, B. J., Bach, H., Sherman, D. H., Lamb, D. C., Kelly, S. L., and Waterman, M. R. (2003) The 1.92 Å structure of *Streptomyces coelicolor* A3(2) CYP154C1. A new monooxygenase that functionalizes macrolide ring systems, *J. Biol. Chem. 278*, 12214−12221.
19. Balkis, M. M., Leidich, S. D., Mukherjee, P. K., and Ghannoum, M. A. (2002) Mechanisms of fungal resistance: An overview, *Drugs 62*, 1025−1049.
20. Souter, A., McLean, K. J., Smith, W. E., and Munro, A. W. (2000) The genome sequence of *Mycobacterium tuberculosis* reveals cytochromes P450 as novel anti-TB drug targets, *J. Chem. Technol. Biotechnol. 75*, 933−941.
21. Bellamine, A., Mangla, A. T., Nes, W. D., and Waterman, M. R. (1999) Characterization and catalytic properties of the sterol 14α-demethylase from *Mycobacterium tuberculosis*, *Proc. Natl. Acad. Sci. U.S.A. 96*, 8937−8942.
22. McLean, K. J., Cheesman, M. R., Rivers, S. L., Richmond, A., Leys, D., Chapman, S. K., Reid, G. A., Price, N. C., Kelly, S. M., Clarkson, J., Smith, W. E., and Munro, A. W. (2002) Expression, purification and spectroscopic characterization of the cytochrome P450 CYP121 from *Mycobacterium tuberculosis*, *J. Inorg. Biochem. 91*, 527−541.
23. Podust, L. M., Poulos, T. L., and Waterman, M. R. (2001) Crystal structure of cytochrome P450 14α-sterol demethylase (CYP51) from *Mycobacterium tuberculosis* in complex with azole inhibitors, *Proc. Natl. Acad. Sci. U.S.A. 98*, 3068−3073.
24. Podust, L. M., Yermalitskaya, L. V., Lepesheva, G. I., Podust, V. N., Dalmasso, E. A., and Waterman, M. R. (2004) Estriol bound and ligand-free structures of sterol 14α-demethylase, *Structure 12*, 1937−1945.
25. Sevrioukova, I. F., Garcia, C., Li, H., Bhaskar, B., and Poulos, T. L. (2003) Crystal structure of putidaredoxin, the [2Fe-2S] component of the P450cam monooxygenase system from *Pseudomonas putida*, *J. Mol. Biol. 332*, 377−392.
26. Sambrook, J., Fritsch, E. F., and Maniatis, T. (1989), in *Molecular Cloning: A Laboratory Manual*, 2nd ed., Cold Spring Harbor Laboratory Press, Plainview, NY.
27. McLean, K. J., Scrutton, N. S., and Munro, A. W. (2003) Kinetic, spectroscopic and thermodynamic characterization of the *Mycobacterium tuberculosis* adrenodoxin reductase homologue FprA, *Biochem. J. 372*, 317−327.
28. Leys, D., Mowat, C. G., McLean, K. J., Richmond, A., Chapman, S. K., Walkinshaw, M. D., and Munro, A. W. (2003) Atomic structure of *Mycobacterium tuberculosis* CYP121 to 1.06 Å reveals novel features of cytochrome P450, *J. Biol. Chem. 278*, 5141−5147.
29. Dutton, P. L. (1978) Redox potentiometry: Determination of midpoint potentials of oxidation−reduction components of biological electron-transfer systems, *Methods Enzymol. 54*, 411−435.
30. Munro, A. W., Noble, M. A., Robledo, L., Daff, S. N., and Chapman, S. K. (2001) Determination of the redox properties of human NADPH-cytochrome P450 reductase, *Biochemistry 40*, 1956−1963.
31. Ost, T. W. B., Miles, C. S., Munro, A. W., Murdoch, J., Reid, G. A., and Chapman, S. K. (2001) Phenylalanine exerts thermodynamic control over the heme of flavocytochrome P450 BM3, *Biochemistry 40*, 13421−13429.
32. Stewart, G. R., Wernisch, L., Stabler, R., Mangan, J. A., Hinds, J., Laing, K. G., Young, D. B., and Butcher, P. D. (2002) Dissection of the heat-shock response in *Mycobacterium tuberculosis* using mutants and microarrays, *Microbiology 148*, 3129−3138.
33. Quaroni, L. G., Seward, H. E., McLean, K. J., Girvan, H. M., Ost, T. W., Noble, M. A., Kelly, S. M., Price, N. C., Cheesman, M. R., Smith, W. E., and Munro, A. W. (2004) Interaction of nitric oxide with cytochrome P450 BM3, *Biochemistry 43*, 16416−16431.
34. Correia, M. A. (2005) Human and rat liver cytochromes P450: Functional markers, diagnostic inhibitor probes, and parameters frequently used in P450 studies, in *Cytochrome P450: Structure, Mechanism and Biochemistry* (Ortiz de Montellano, P. R., Ed.) 3rd ed., pp 619−657, Kluwer Academic/Plenum Publishers, New York.
35. Berry, E. A., and Trumpower, B. L. (1987) Simultaneous determination of hemes-a, hemes-b, and hemes-c from pyridine hemochrome spectra, *Anal. Biochem. 161*, 1−15.
36. Hawkes, D. B., Adams, G. W., Burlingame, A. L., Ortiz de Montellano, P. R., and De Voss, J. J. (2002) Cytochrome $P450_{cin}$ (CYP176A), isolation, expression, and characterization, *J. Biol. Chem. 277*, 27725−27732.
37. Matsuura, K., Yoshioka, S., Tosha, T., Hori, H., Ishimori, K., Kitagawa, T., Morishima, I., Kagawa, N., and Waterman, M. R. (2005) Structural diversities of active site in clinical azole-bound forms between sterol 14α-demethylases (CYP51s) from human and *Mycobacterium tuberculosis*, *J. Biol. Chem. 280*, 9088−9096.
38. Sreerama, N., and Woody, R. W. (2000) Analysis of protein CD spectra: Comparison of CONTIN, SELCON 3 and CDSSTR methods in Cdpro software, *Anal. Biochem. 287*, 252−260.
39. Sevrioukova, I. F. (2005) Redox-dependent structural reorganization in putidaredoxin, a vertebrate-type [2Fe-2S] ferredoxin from *Pseudomonas putida*, *J. Mol. Biol. 347*, 607−621.
40. Trower, M. K., Lenstra, R., Omer, C., Buchholz, S. E., and Sariaslani, F. S. (1992) Cloning, nucleotide sequence determination and expression of the genes encoding cytochrome P-450soy (soyC) and ferredoxinsoy (soyB) from *Streptomyces griseus*, *Mol. Microbiol. 6*, 2125−2134.
41. Green, A. J., Munro, A. W., Cheesman, M. R., Reid, G. A., von Wachenfeldt, C., and Chapman, S. K. (2003) Expression, purification and characterisation of a *Bacillus subtilis* ferredoxin: A potential electron transfer donor to cytochrome P450 BioI, *J. Inorg. Biochem. 93*, 92−99.
42. Holden, M., Mayhew, M., Bunk, D., Roitberg, A., and Vilker, V. (1997) Probing the interactions of putidaredoxin with redox partners in camphor P450 5-monooxygenase by mutagenesis of surface residues, *J. Biol. Chem. 272*, 21720−21725.
43. Cammack, R. (1992) Iron−sulfur clusters in enzymes: Themes and variations, *Adv. Inorg. Chem. 38*, 281−322.
44. Beinert, H., and Kennedy, M. C. (1989) Engineering of protein-bound iron−sulfur clusters: A tool for the study of protein and cluster chemistry and mechanism of iron−sulfur enzymes, *Eur. J. Biochem. 186*, 5−15.
45. Thomson, A. J. (1993) Iron−sulfur proteins: Cross-linked by a cluster, *Curr. Biol. 3*, 173−174.
46. Johnson, M. K., Thomson, A. J., Richards, A. J. M., Peterson, J., Robinson, A. E., Ramsay, R. R., and Singer, T. P. (1984) Characterization of the Fe−S cluster in aconitase using low-temperature magnetic circular dichroism spectroscopy, *J. Biol. Chem. 259*, 2274−2282.
47. Cheesman, M. R., Greenwood, C., and Thomson, A. J. (1991) Magnetic Circular Dichroism of Hemoproteins, *Adv. Inorg. Chem. 36*, 201−255.
48. Aoyama, Y., Horiuchi, T., Gotoh, O., Noshiro, M., and Yoshida, Y. (1998) CYP51-like gene of *Mycobacterium* tuberculosis actually encodes a P450 similar to eukaryotic CYP51, *J. Biochem. 124*, 694−696.
49. Ogura, H., Nishida, C. R., Hoch, U. R., Perera, R., Dawson, J. H., and Ortiz de Montellano, P. R. (2004) EpoK, a cytochrome P450 involved in biosynthesis of the anticancer agents epothilones

A and B. Substrate-mediated rescue of a P450 enzyme, *Biochemistry 43*, 14712−14721.
50. Yoshida, Y., and Aoyama, Y. (1984) Yeast cytochrome P-450 catalyzing lanosterol 14α-demethylation. I. Purification and spectral properties, *J. Biol. Chem. 259*, 1655−1660.
51. Jackson, C. J., Lamb, D. C., Marczylo, T. H., Warrilow, A. G., Manning, N. J., Lowe, D. J., Kelly, D. E., and Kelly, S. L. (2002) A novel sterol 14α-demethylase/ferredoxin fusion protein (MCCYP-51FX) from *Methylococcus capsulatus* represents a new class of the cytochrome P450 superfamily, *J. Biol. Chem. 277*, 46959−46965.
52. McKnight, J. E., Cheesman, M. R., Cheesman, M. R., Thomson, A. J., Miles, J. S., and Munro, A. W. (1993) Identification of charge-transfer transitions in the optical spectrum of low-spin ferric cytochrome P-450 *Bacillus megaterium*, *Eur. J. Biochem. 213*, 683−687.
53. Cheesman, M. R., Little, P. J., and Berks, B. C. (2001) Novel heme ligation in a *c*-type cytochrome involved in thiosulfate oxidation: EPR and MCD of SoxAX from *Rhodovulum sulfidophilum*, *Biochemistry 40*, 10562−10569.
54. Dhawan, I. K., Shelver, D., Thorsteinsson, M. V., Roberts, G. P., and Johnson, M. K. (1999) Probing the heme axial ligation in the CO-sensing CooA protein with magnetic circular dichroism spectroscopy, *Biochemistry 38*, 12805−12813.
55. Daff, S. N., Chapman, S. K., Turner, K. L., Holt, R. A., Govindaraj, S., Poulos, T. L., and Munro, A. W. (1997) Redox control of the catalytic cycle of flavocytochrome P-450 BM3, *Biochemistry 36*, 13816−13823.
56. Sligar, S. G. (1976) Coupling of spin, substrate, and redox equilibria in cytochrome P450, *Biochemistry 15*, 5399−5406.
57. Ost, T. W. B., Miles, C. S., Munro, A. W., Murdoch, J., Reid, G. A., and Chapman, S. K. (2001) Phenylalanine 393 exerts thermodynamic control over the heme of flavocytochrome P450 BM3, *Biochemistry 40*, 13421−13429.
58. Perera, R., Sono, M., Sigman, J. A., Pfister, T. D., Lu, Y., and Dawson, J. H. (2003) Neutral thiol as a proximal ligand to ferrous heme iron: Implications for heme protins that lose thiolate ligation on reduction, *Proc. Natl. Acad. Sci. U.S.A. 100*, 3641−3646.
59. McIver, L., Leadbeater, C., Campopiano, D. J., Baxter, R. L., Daff, S. N., Chapman, S. K., and Munro, A. W. (1998) Characterisation of flavodoxin $NADP^+$ oxidoreductase and flavodoxin: Key components of electron transfer in *Escherichia coli*, *Eur. J. Biochem. 257*, 577−585.
60. Ogura, H., Nishida, C. R., Hoch, U. R., Perera, R., Dawson, J. H., and Ortiz de Montellano, P. R. (2004) EpoK, a cytochrome P450 involved in biosynthesis of the anticancer agents epothilones A and B. Substrate-mediated rescue of a P450 enzyme, *Biochemistry 43*, 14712−14721.
61. Poulos, T. L., and Howard, A. J. (1987) Crystal structures of metyrapone- and phenylimidazole-inhibited complexes of cytochrome P-450cam, *Biochemistry 26*, 8165−8174.
62. Munro, A. W., Lindsay, J. G., Coggins, J. R., Kelly, S. M., and Price, N. C. (1996) Analysis of the structural stability of the multidomain enzyme flavocytochrome P-450 BM3, *Biochim. Biophys. Acta 1296*, 127−137.
63. Tschirret-Guth, R. A., Koo, L. S., Hoa, G. H., and Ortiz de Montellano, P. R. (2001) Reversible pressure deformation of a thermophilic cytochrome P450 enzyme (CYP119) and its active-site mutants, *J. Am. Chem. Soc. 123*, 3412−3417.
64. Cheesman, M. J., Baer, B. R., Zheng, Y.-M., Gillam, E. M. J., and Rettie, A. E. (2003) Rabbit CYP4B1 engineered for high-level expression in *Escherichia coli*: Ligand stabilization and processing of the N-terminus and heme prosthetic group, *Arch. Biochem. Biophys. 416*, 17−24.
65. Yeh, H.-C., Hsu, P.-Y., Wang, J.-S., Tsai, A.-L., and Wang, L.-H. (2005) Characterization of heme environment and mechanism of peroxide bond cleavage in human prostacyclin synthase, *Biochim. Biophys. Acta 1738*, 121−132.
66. Berka, V., Palmer, G., Chen, P.-F., and Tsai, A.-L. (1998) Effects of various imidazole ligands on heme conformation in endothelial nitric oxide synthase, *Biochemistry 37*, 6136−6144.
67. Gatfield, J., and Pieters, J. (2000) Essential role for cholesterol in the entry of mycobacteria into macrophages, *Science 288*, 1647−1650.
68. Miles, A. W., Munro, A. W., Rospendowski, B. N., Smith, W. E., McKnight, J. E., and Thomson, A. J. (1992) Domains of the catalytically self-sufficient cytochrome P-450 BM-3: Genetic construction, overexpression, purification and spectroscopic characterization, *Biochem. J. 288*, 503−509.
69. Cole, P. E., and Sligar, S. G. (1981) Temperature jump measurement of the spin state relaxation rate of cytochrome $P450_{cam}$, *FEBS Lett. 133*, 252−254.
70. Dawson, J. H., Andersson, L. A., and Sono, M. (1982) Spectroscopic investigations of ferric cytochrome P-450-Cam ligand complexes: Identification of the ligand trans to cysteinate in the native enzyme, *J. Biol. Chem. 257*, 3606−3617.
71. Sono, M., and Dawson, J. H. (1982) Formation of low-spin complexes of ferric cytochrome P-450-Cam with anionic ligands: Spin state and ligand affinity comparison to myoglobin, *J. Biol. Chem. 257*, 5496−5502.
72. O'Keeffe, D. H., Ebel, R. E., and Peterson, J. A. (1978) Studies of the oxygen binding site of cytochrome P-450. Nitric oxide as a spin-label probe, *J. Biol. Chem. 253*, 3509−3516.
73. Yoshioka, S., Tosha, T., Takahashi, S., Ishimori, K., Hori, H., and Morishima, I. (2002) Roles of the proximal hydrogen bonding network in cytochrome P450cam-catalyzed oxygenation, *J. Am. Chem. Soc. 124*, 14571−14579.
74. O'Keefe, D. P., Gibson, K. J., Emptage, M. H., Lenstra, R., Romesser, J. A., Litle, P. J., and Omer, C. A (1991) Ferredoxins from two sulfonylurea herbicide monooxygenase systems in *Streptomyces griseolus*, *Biochemistry 30*, 447−455.
75. Gunsalus, I. C., and Wagner, G. C. (1978) Bacterial P-450cam methylene monooxygenase components: Cytochrome m, putidaredoxin, and putidaredoxin reductase, *Methods Enzymol. 52*, 166−188.
76. Shimada, H., Nagano, S., Hori, H., and Ishimura, Y. (2001) Putidaredoxin-cytochrome P450cam interaction, *J. Inorg. Biochem. 83*, 255−260.
77. Sligar, S. G., and Gunsalus, I. C. (1976) A thermodynamic model of regulation: Modulation of redox equilibria in camphor monooxygenase, *Proc. Natl. Acad. Sci. U.S.A. 73*, 1078−1082.

BI0601609